Cell

The extracellular matrix integrates mitochondrial homeostasis

Graphical abstract

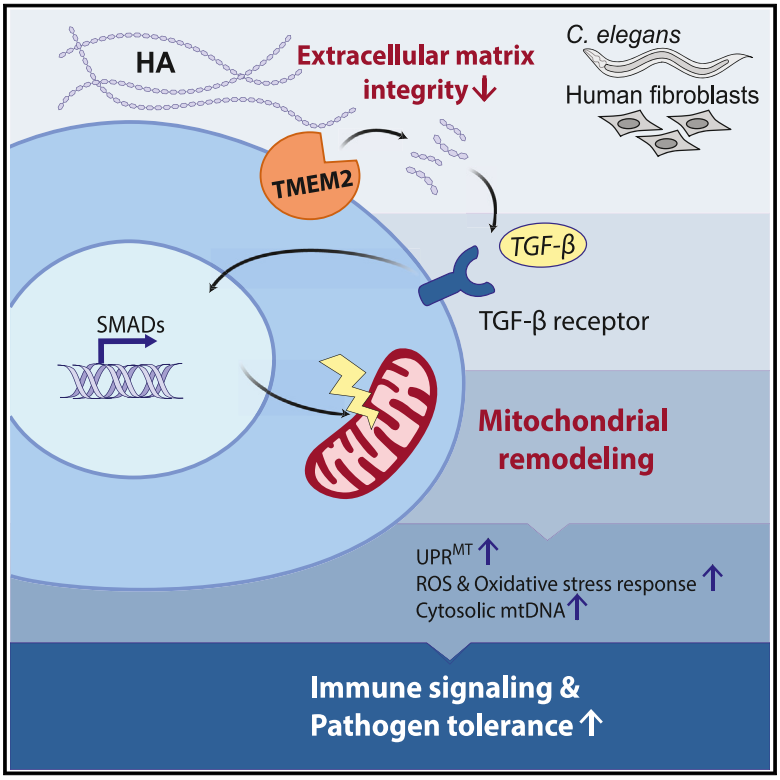

Highlights

- Hyaluronan degradation in the ECM induces mitochondrial remodeling
- This ECM-to-mitochondria communication pathway is evolutionarily conserved
- The TGF-β signaling mediates the ECM-to-mitochondria communication
- ECM remodeling promotes immunity through the TGF-β and mitochondrial signaling

Authors

Hanlin Zhang, C. Kimberly Tsui, Gilberto Garcia, ..., Phillip A. Frankino, Ryo Higuchi-Sanabria, Andrew Dillin

Correspondence

dillin@berkeley.edu

In brief

Degradation of hyaluronan in the extracellular matrix leads to mitochondrial remodeling, activation of mitochondrial stress responses, and augmented immune signaling.

Zhang et al., 2024, Cell *187*, 4289–4304
August 8, 2024
https://doi.org/10.1016/j.cell.2024.05.057

CellPress

Cell

CellPress

Article

The extracellular matrix integrates mitochondrial homeostasis

Hanlin Zhang,[1] C. Kimberly Tsui,[1] Gilberto Garcia,[1,2] Larry K. Joe,[1] Haolun Wu,[1] Ayane Maruichi,[1] Wudi Fan,[1] Sentibel Pandovski,[1] Peter H. Yoon,[1] Brant M. Webster,[1] Jenni Durieux,[1] Phillip A. Frankino,[1] Ryo Higuchi-Sanabria,[1,2] and Andrew Dillin[1,3,*]

[1]Department of Molecular & Cell Biology, Howard Hughes Medical Institute, University of California, Berkeley, Berkeley, CA 94720, USA
[2]Present address: Leonard Davis School of Gerontology, University of Southern California, Los Angeles, CA 90089, USA
[3]Lead contact
*Correspondence: dillin@berkeley.edu
https://doi.org/10.1016/j.cell.2024.05.057

SUMMARY

Cellular homeostasis is intricately influenced by stimuli from the microenvironment, including signaling molecules, metabolites, and pathogens. Functioning as a signaling hub within the cell, mitochondria integrate information from various intracellular compartments to regulate cellular signaling and metabolism. Multiple studies have shown that mitochondria may respond to various extracellular signaling events. However, it is less clear how changes in the extracellular matrix (ECM) can impact mitochondrial homeostasis to regulate animal physiology. We find that ECM remodeling alters mitochondrial homeostasis in an evolutionarily conserved manner. Mechanistically, ECM remodeling triggers a TGF-β response to induce mitochondrial fission and the unfolded protein response of the mitochondria (UPR^{MT}). At the organismal level, ECM remodeling promotes defense of animals against pathogens through enhanced mitochondrial stress responses. We postulate that this ECM-mitochondria crosstalk represents an ancient immune pathway, which detects infection- or mechanical-stress-induced ECM damage, thereby initiating adaptive mitochondria-based immune and metabolic responses.

INTRODUCTION

Cells are continually having to sense and communicate aspects of their extracellular environment to the inside of the cell. Many of these sensing mechanisms require ligand-receptor interactions at the plasma membrane to elucidate the proper cellular response. However, each cell is coated with the extracellular matrix (ECM), composed of proteins and large carbohydrates that may sequester soluble biochemical signals to regulate the ligand-receptor interactions.[1] In fact, the ECM can reach 500 nm thick on the endothelial surface to 20 μm thick in connective tissues, which excludes macromolecules and poses a barrier on ligand-receptor interaction, especially those involving detection of pathogen and damage.[2,3] Therefore, could there be communication events dictated from the ECM to inform the inside of the cell about possible challenges on the outside of the cell? If so, what could be the source of this communication, what is communicated, and, finally, what changes on the inside of the cell are created to match the external challenges? In this study, we applied genetic and pharmaceutical approaches to remodel the ECM in mammalian cells and *C. elegans*, unraveling the molecular mechanisms of an ECM-mitochondria communication pathway and the physiological significance of this intercellular compartment communication in live animals.

By definition, the ECM is the composite accumulation of various types of structural and functional molecules that are secreted by all cell types.[4] As the major component of the extracellular microenvironment, where intercellular and host-microbiome communications occur, the ECM is a frequent target of viruses, bacteria, and fungi to achieve successful adhesion, invasion, and pathogenesis.[5] For example, the human opportunistic pathogenic bacteria *E. faecalis* expresses multiple adhesins, such as collagen-binding proteins, and invasins, such as hyaluronidases and gelatinases, which contribute to their virulence.[6,7]

Hyaluronan (hyaluronic acid [HA]) is a non-sulfated glycosaminoglycan (GAG) that is a major component of the mammalian ECM.[8] It is a linear polymer composed of repeating disaccharide units of glucuronic acid and *N*-acetyl-glucosamine. Under steady conditions, HA exists in a high-molecular-weight (HMW) format reaching 2,000 kDa, approximately 6,000 disaccharide units in human tissues.[9] HA fibers maintain structural integrity of the ECM and regulate cellular behaviors, such as migration and repair.[10] The size and amount of HA fibers deposited in the ECM is a balanced outcome between activities of hyaluronan synthases and hyaluronidases.[8] Transmembrane protein 2 (TMEM2) is a major cell-surface hyaluronidase that degrades HMW HA into low-molecular-weight (LMW) ~5 kDa fragments.[11–13] Notably, TMEM2's

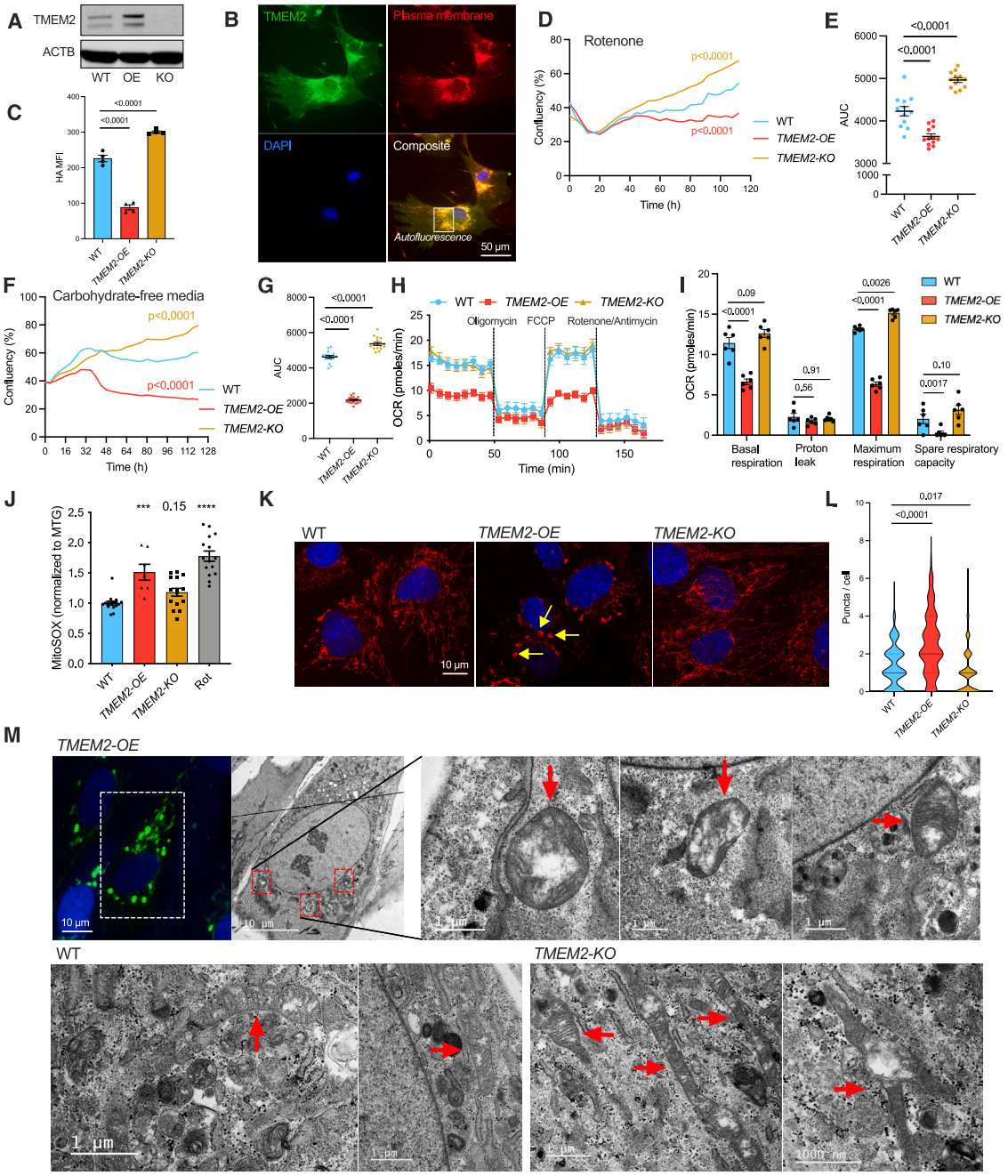

Figure 1. TMEM2-mediated ECM remodeling results in altered mitochondrial function

(A) The protein levels of TMEM2 in wild-type (WT), *TMEM2-OE*, and *TMEM2-KO* BJ fibroblasts were measured by western blot.

(B) WT fibroblasts expressing *GFP-TMEM2* were stained with the plasma membrane dye wheat germ agglutinin-AF647 (WGA-AF647) and DAPI and imaged with a fluorescence microscope.

(C) Cell-surface hyaluronan was stained with HABP and quantified using flow cytometry. $n = 4$.

(D–G) Cells of indicated genotypes were treated with rotenone and their growth was monitored using live-cell imaging by Incucyte (D). Area under curve (AUC) values were calculated for statistical analyses (E). Similarly, cells were grown in carbohydrate-free (CF) media (F) and growth curves compared using AUC values (G). $n = 12$ for (E) and 16 for (G).

(H and I) The cellular oxygen consumption rates under basal or drug-treated conditions were measured using Seahorse (H) and quantified in (I). $n = 6$.

(J) Mitochondrial ROS levels were measured using MitoSOX flow cytometry staining. Values were normalized to mitochondrial mass, as quantified by MitoTracker Green (MTG) staining. $n = 7–16$, as indicated by individual dots.

(legend continued on next page)

cleavage activity is specific to non-sulfated HA and does not cleave other sulfated GAGs.[11] Besides degradation caused by pathogen-derived external hyaluronidases,[14] accelerated degradation of HA is found in other pathologic conditions, including rheumatoid arthritis, diabetes, cancer, and inflammation,[10,15] possibly caused by altered cellular HA metabolism. As such, HA degradation is a key marker and contributing catalyst in the progression of diseases, but its precise implications for cellular physiology are unknown.

In addition to providing mechanical support for the cell, the ECM also functions as a reservoir of signaling molecules. Although HA has a relatively simple structure, a variety of HA-binding proteins (HABPs) have been identified, such as CD44 and Toll-like receptor 4 (TLR4), whose activities may be affected upon binding to HA.[16] Specifically, LMW HA fragments are pro-inflammatory and trigger cell migration and proliferation, whereas HMW HA promotes anti-inflammatory and antiproliferative effects.[17–19] Besides molecules directly derived from cleavage of large ECM polymers, small secreted signaling molecules, such as growth factors and cytokines, are found—and sometimes even enriched—in the ECM.[20] As a result, disturbance of the ECM can modulate the signaling activities of these molecules. For example, transforming growth factor β (TGF-β) ligands are secreted and stored in the ECM in their latent forms. Upon mechanical or biochemical stimuli that disrupts the ECM,[21,22] TGF-β ligands are activated and signal via the downstream SMAD pathways to initiate a series of cellular responses, such as proliferation, differentiation, apoptosis, and ECM deposition.[23]

Although the ECM can coordinate signaling events outside of the cell, mitochondria are crucial signaling hubs inside of the cell. Mitochondria direct cellular metabolism, stress responses, innate immunity, and cell death.[24] Orchestrating mitochondrial homeostasis involves intricate mechanisms, including balanced expression of mitochondrial genes encoded by the nuclear and mitochondrial genomes, mitochondrial fission and fusion, mitochondrial stress responses—including the unfolded protein response of the mitochondria (UPR^{MT})[25–28] and the oxidative stress response[29,30] that restore mitochondrial homeostasis via promoting transcription of cellular homeostatic proteins—and mitophagy, which removes damaged mitochondria. Activation of mitochondrial stress responses enhance organismal resistance to environmental stress and aging.[29,31,32] The concept of leveraging mild mitochondrial stress, known as mitohormesis, to trigger protective responses for improved resilience has garnered extensive attention.[33] Alongside mitochondrial toxins, physiological inducers of mitochondrial stress include mitochondrial permeability changes,[34] mitochondrial gene mutations, and oxidative damage.[35] Besides intracellular stimuli, mitochondrial form and function could also align with cellular behavior adjustments prompted by extracellular stimuli. Several pioneering studies showed that the integrin-signaling pathway, which is key to converting mechanical cues from the ECM into intracellular signaling cascades, stimulates mitochondrial stress signaling through mediators like focal adhesion kinase (FAK).[36,37]

RESULTS

TMEM2-mediated ECM remodeling results in altered mitochondrial function in human cells

HA is a major GAG component pivotal for preserving the integrity and functionality of the mammalian ECM. To modulate HA homeostasis, we conducted both overexpression (OE) and knockout (KO) of the hyaluronidase *TMEM2* in human fibroblasts, a cell type that generates and secretes a large amount of ECM components, including HA (Figures 1A, S1A, and S1B), and is a sentinel that controls local immune responses during infection.[38] TMEM2 localizes on the plasma membrane of fibroblasts (Figure 1B). OE or KO of *TMEM2* is sufficient to reduce or increase the amount of HA in the ECM, as assessed by HA-flow cytometry staining (Figure 1C) in cell lysates (Figure S1C), and in conditioned culture media (Figure S1D), as assessed by HA-ELISA, which is in line with its reported function as a cell-surface hyaluronidase that cleaves extracellular HA.[11] Previous studies found that TMEM2 impacts cellular resistance against the endoplasmic reticulum (ER) stress inducer tunicamycin without affecting ER stress pathways,[39] indicating that TMEM2 may regulate cellular homeostasis through an unknown mechanism. To assess how TMEM2-induced ECM remodeling may impact cellular homeostasis, we performed a series of stress resistance assays by treating cells with different stress inducers and measuring their growth using the Incucyte Live-cell Analysis System (Figures S1E and S1F). This dynamic growth-based assay is a highly quantitative physiological readout for measuring cellular resilience against different types of stress across a long period of time, and hence may reflect the quality of different cellular compartments.[40] As a proof of concept, KO of the nuclear encoded mitochondrial electron transport chain genes, *COX11* or *SDHD*, resulted in cells more sensitive to mitochondrial stress through exposure to rotenone (Figures S1G–S1I) or carbohydrate-free (CF) media (Figures S1J and S1K). Interestingly, alteration of the ECM, by OE of *TMEM2*, also resulted in cells more sensitive to rotenone (Figures 1D and 1E) and CF media (Figures 1F, 1G, and S1L). Additionally, *TMEM2-OE* cells were also sensitive to a variety of other mitochondrial stress conditions, including low-glucose media (Figure S1M), galactose media (Figure S1N), NaN_3 treatment that inhibits complex IV activity (Figure S1O), and the oxidative stress inducer H_2O_2 (Figure S1P). In contrast, *TMEM2-KO* cells were more resistant to these mitochondrial stress conditions (Figures 1D–1G and S1L). As a complementary approach to test whether HA remodeling in the ECM can lead to mitochondrial stress, we treated *TMEM2-KO* cells

(K and L) Cells were stained with MitoTracker Deep Red (MTDR) and imaged using an Airyscan confocal microscope (K). Mitochondrial puncta numbers were quantified using a Fiji program (L). n = 130–150 cells.

(M) Correlative light electron microscopy was performed on cells of indicated genotypes. Mitochondria are labeled out with red arrows.

Data represented as mean ± SEM (C, E, and G–J), mean (D and F), or median ± interquartile range (L). One-way or two-way ANOVA with post hoc Dunnett's test (C, E, G, I, and J) or Kruskal-Wallis test with post hoc Dunn's test (L).

See also Figure S1.

with purified hyaluronidase and found that exogenous hyaluronidase treatment was sufficient to sensitize cells to rotenone (Figure S1Q). Moreover, overexpressing *TMEM2* in *TMEM2-KO* cells also re-sensitized them to mitochondrial stress (Figures S1R–S1U). Finally, we found little difference with stressors of the Golgi or the actin cytoskeleton (Figures S1V and S1W) or inhibitors of general transcription or translation (Figures S1X and S1Y).

Intrigued by the finding that alterations of the ECM sensitized cells to mitochondrial stress, we hypothesized that mitochondrial homeostasis might also be affected. Indeed, *TMEM2-OE* cells had a significant reduction of mitochondrial respiration rates, including both basal and maximal respiration (Figures 1H and 1I), which was associated with a slightly increased rate of glycolysis (Figure S1Z). Moreover, *TMEM2-OE* cells had increased mitochondrial reactive oxygen species (ROS) (Figure 1J), and mildly reduced cellular ATP levels (Figure S1AA). However, mitochondrial mass was not markedly altered in *TMEM2-OE* cells, as assessed by both mitochondrial-protein ATP5A western blot analysis and MitoTracker Green flow cytometry staining (Figures S1AB–AD). The nicotinamide adenine dinucleotide/nicotinamide adenine dinucleotide hydrogen (NAD/NADH) ratio was not altered in *TMEM2-OE* cells either (Figure S1AE). *TMEM2-KO* cells did not have obvious functional enhancements compared with wild-type cells (Figures 1H and 1I), which may be due to already-optimal mitochondrial functions in wild-type cells.

To gain a more direct understanding of mitochondrial changes occurring in *TMEM2-OE* and *TMEM2-KO* cells, mitochondrial morphology was analyzed using Airyscan confocal super-resolution microscopy. Surprisingly, mitochondria in *TMEM2-OE* cells form many enlarged puncta structures comparing to wild-type cells, whereas mitochondria in *TMEM2-KO* cells are more tubular and form very few puncta (Figures 1K and 1L). Similar changes to mitochondrial morphology were observed in two more *TMEM2-KO* clones generated by different single-guide RNA (sgRNA) sequences (Figure S1AF). We then tested whether the mitochondrial puncta found in *TMEM2-OE* cells were mitophagy-digested mitochondrial aggregates. To do so, we tested whether lysosomes, by following the lysosomal protein, lysosomal-associated membrane protein 1 (LAMP1), colocalized with the mitochondrial puncta. Very little co-localization was found (Figure S1AG). Next, correlative light and electron microscopy (CLEM) was performed to directly image these mitochondrial structures at nanometer resolution. CLEM analysis revealed that the puncta in *TMEM2-OE* cells are swollen individual mitochondria (Figure 1M), consistent with mitochondrial hyperfission phenotypes found by electron microscopy.[41,42] By contrast, *TMEM2-KO* cells had more elongated and branched mitochondria (Figure 1M), indicating hyper-fused mitochondria. To test whether increased oxidative stress is a cause of mitochondrial fission in *TMEM2-OE* cells, antioxidants N-acetyl-L-cysteine (NAC) and 10-(6′-plastoquinonyl)decyltriphenylphosphonium (SKQ1) were supplemented. Indeed, exacerbated mitochondrial fission was observed under these treatments (Figure S1AH), indicating that an alternative mechanism other than oxidative stress may exist to drive mitochondrial morphological changes in *TMEM2-OE* cells. Taken together, *TMEM2-OE*-induced ECM remodeling in human cells leads to increased mitochondrial fragmentation, declined mitochondrial respiration, increased mitochondrial oxidative stress, and increased sensitivity to mitochondrial stress.

ECM remodeling results in altered mitochondrial function in *C. elegans*

The ECM is a pivotal structure for environmental sensing and intercellular communication, and the major ECM components are conserved from invertebrates to humans.[43] Therefore, it is possible that this phenomenon of ECM-mitochondria communication is conserved across species. To test this hypothesis, we ectopically overexpressed human *TMEM2* (*hTMEM2*) in *C. elegans* and compared their transcriptome with wild-type animals. Multiple mitochondrial-stress-related pathways, including the UPR^{MT}, were activated by hTMEM2 (Figure S2A). As an additional measure of mitochondrial stress responses induced by *hTMEM2* OE, we tested whether *hTMEM2-OE* could ectopically induce a known reporter gene of the UPR^{MT}, heat shock protein hsp-6 (*hsp-6*), using animals expressing the *hsp-6p::GFP* UPR^{MT} reporter. OE of *hTMEM2* significantly increased the expression of the *hsp-6p::GFP* reporter, as assessed by fluorescence microscopy and quantified using a large particle flow cytometer (Figures 2A, 2B, and S2B–S2D). Importantly, OE of a mutated version of TMEM2 lacking the HA depolymerization activity had no impact on the UPR^{MT} activity (Figures 2A and 2B),[11,39] suggesting that hTMEM2 induces the UPR^{MT} by degrading components of the *C. elegans* ECM. Furthermore, *hTMEM2* OE induces *hsp-6* expression in an *atfs-1*-dependent manner (Figures S2E and S2F) and results in robust induction and nuclear localization of DVE-1 (Figure 2C), hallmarks of *bona fide* UPR^{MT} induction.[27]

The major GAG component of the ECM in *C. elegans* is chondroitin, an isomer of HA that is nearly identical except for the stereochemistry of the C-4 hydroxyl group on the hexosamine moiety (Figure 2D).[44] Notably, many known hyaluronidases and chondroitinases exhibit overlapping substrate specificities.[45] OE of *TMEM2* resulted in less chondroitin (Figures 2E and 2F). Likewise, the *C. elegans* gene *chhy-1* encodes a chondroitinase.[46] Similar to OE of *TMEM2*, OE of *chhy-1* reduced chondroitin levels (Figures 2E and 2F) and also induced the UPR^{MT} (Figures 2G and 2H). Therefore, it is possible that hTMEM2 may operate as a chondroitinase in *C. elegans*, with CHHY-1 being its functional homolog, although this requires more direct biochemical assays to confirm.

To evaluate ECM-induced mitochondrial changes in *C. elegans*, we assessed the impact of *hTMEM2-OE* on mitochondrial morphology. Interestingly, *hTMEM2-OE* had no impact on mitochondrial morphology in young adult animals (Figures S2G and S2H). However, aged *hTMEM2-OE* animals exhibited pronounced mitochondrial fragmentation in comparison with wild-type N2 animals (Figures 2I and 2J). Consistent with observations in human cells, the oxygen consumption rate (OCR) also declined in *hTMEM2-OE* animals (Figure 2K).

Mitochondria are a major origin of cellular ROS, thereby frequently triggering oxidative stress and the accompanying oxidative stress responses amid mitochondrial perturbations. In *C. elegans*, SKN-1, the ortholog of mammalian NRF2, is the

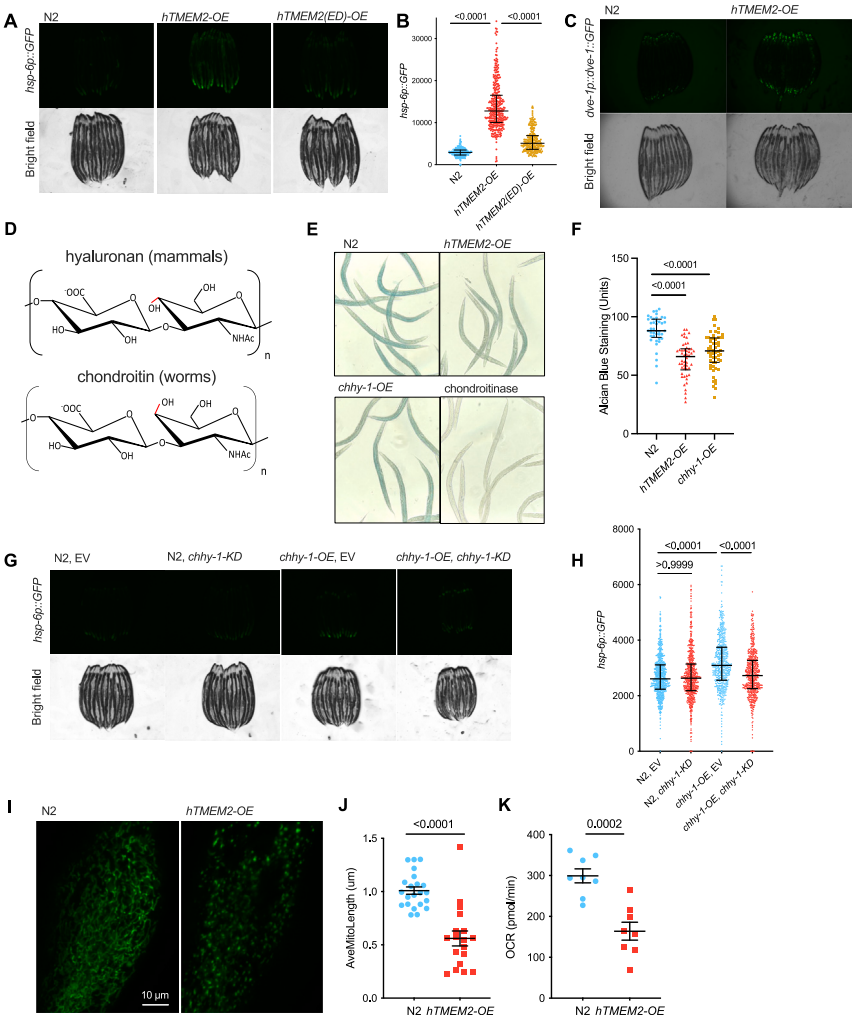

Figure 2. ECM remodeling results in altered mitochondrial function in *C. elegans*

(A and B) *hTMEM2-OE* (*sur-5p::hTMEM2*) or enzymatically dead (ED) *hTMEM2-OE* animals were crossed with the *hsp-6p::GFP* UPR^{MT} reporter strain, and their GFP measured by fluorescence microscopy (A) and a worm sorter (B). *N* = 200–350.

(C) *hTMEM2-OE, dve-1p::dve-1::GFP* reporter animals were imaged using a fluorescence microscope.

(D) Comparison of the basic structure between hyaluronan and chondroitin.

(E and F) WT, *chhy-1-OE* (*chhy-1p::chhy-1*), or *hTMEM2-OE* animals were grown to the L4 stage and stained with Alcian blue. Images were taken with a color sensor-equipped Revolve microscope (E) and quantified using FIJI (F). *n* = 40–50.

(G and H) Animals of indicated genotypes were crossed with *hsp-6p::GFP* reporter animals and grown on EV or *chhy-1* RNAi bacteria for GFP measurement using fluorescence microscopy (G) and a worm sorter (H). *n* = 564–792.

(I and J) *hTMEM2-OE, vha-6p::MLS::GFP* mitochondrial reporter animals were imaged using an Airyscan confocal microscope at the age of day 13 (I). Individual mitochondrial length was measured using FIJI (J). *n* = 18–22.

(K) OCR of live animals were measured using Seahorse. *n* = 8.

Data represented as median ± interquartile range (B, F, and H) or mean ± SEM (J and K). Kruskal-Wallis test with post hoc Dunn's test (B, F, and H), Welch's t test (J), or Student's t test (K).

See also Figure S2.

key transcription factor that regulates oxidative stress responses. Using the SKN-1 target gene, *gst-4*, as a reporter, we found that wild type but not mutated hTMEM2 elicited an oxidative stress response in a *skn-1*-dependent manner (Figures S2I–S2L), in alignment with our RNA sequencing (RNA-seq) findings (Figure S2A). Moreover, by crossing with the hypoxia-inducible factor 1 (HIF-1) reporter strain *cysl-2p::Venus*,[47] we found that the HIF-1 signaling pathway was not potently induced by hTMEM2 (Figures S2M and S2N).

Taken together, hTMEM2 induces similar mitochondrial functional declines as well as mitochondrial stress responses in *C. elegans* and human cells, indicating that this phenomenon of ECM-mitochondria communication may have arisen early in evolution.

The TGF-β receptor mediates communication between the ECM and mitochondria

To uncover how changes in the ECM are communicated inside of the cell to alter mitochondrial form and function, we performed a CRISPR-KO screen targeting 2,073 genes encoding proteins located on the plasma membrane (Table S1). This library included ECM fibrous components such as collagens and elastin, proteoglycans that bind to or regulate ECM fiber, and cell-surface receptors pivotal for transducing signals from the extracellular milieu, including HA-binding proteins. Following library transduction into Cas9-expressing wild-type or *TMEM2-OE* cells, we performed growth selection using rotenone or CF media to which *TMEM2-OE* cells are sensitive (Figure 3A). Therefore, any genes identified in this CRISPR-KO screen would be expected to play a role in communication from the ECM to mitochondria.

As anticipated, the outcomes from rotenone- and CF-media-mediated selections were highly congruent (Figures S3A and S3B), substantiating the robustness of this approach. To identify the signaling pathway downstream of TMEM2, we primarily focused on the signaling receptor subgroup of genes found in this screen. Multiple hits were identified whose KO improved the resistance of *TMEM2-OE* cells to rotenone and/or CF media (Figure 3B). Particularly intriguing were both subunits of the TGF-β receptor, TGFBR1, and TGFBR2 (Figure 3B) because the TGF-β signaling pathway is highly conserved from *C. elegans* to mammals and plays a central role in sensing and regulating ECM remodeling as introduced earlier.[21–23] We validated that knocking out TGFBR1 or TGFBR2 was sufficient to rescue the growth deficiency phenotype of *TMEM2-OE* cells under conditions of

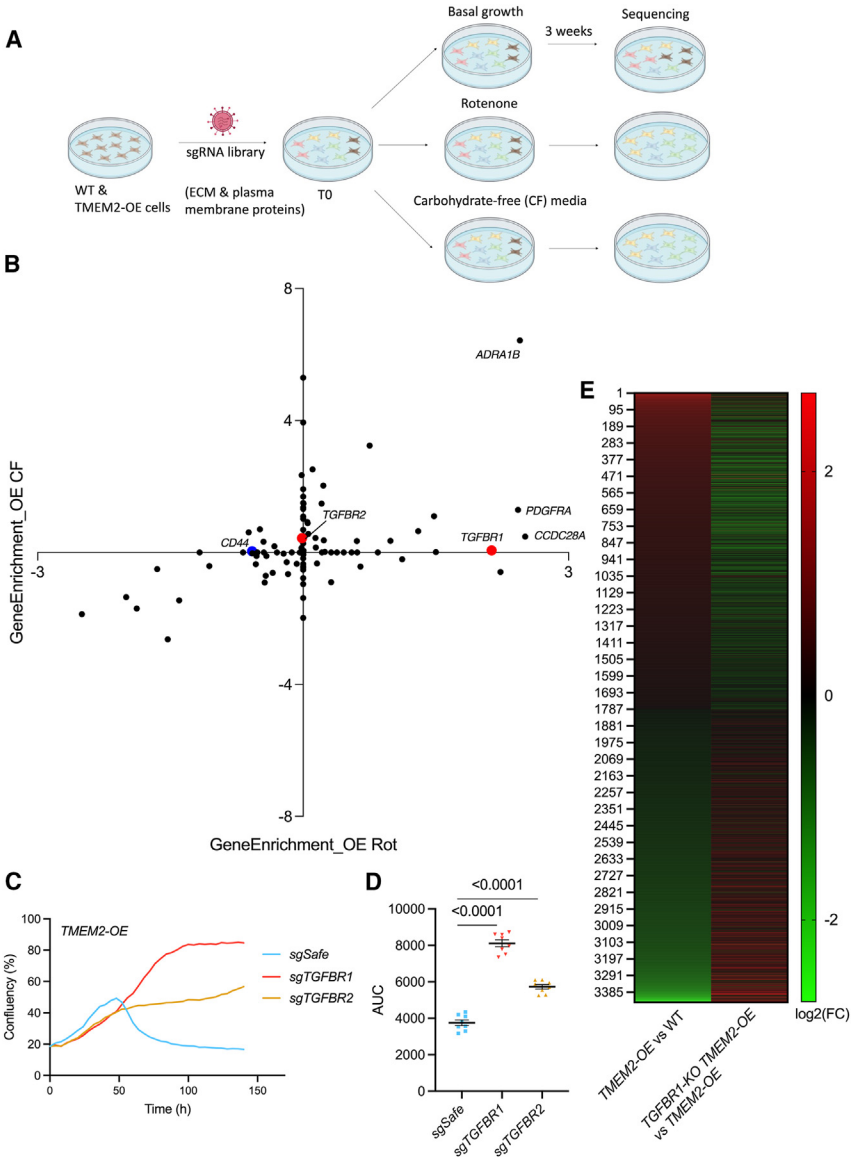

Figure 3. The TGF-β receptor mediates communication between the ECM and mitochondria

(A) Cas9-expressing WT or *TMEM2-OE* cells were transduced with the sgRNA library and selected under basal or mitochondrial stress conditions for 3 weeks, followed by sequencing analyses.

(B) Comparison of gene enrichment scores between CF- and rotenone-selected cells. The transmembrane signal receptor genes of *TMEM2-OE* cells are selectively shown. *TGFBR1* and *TGFBR2* are highlighted in red.

(C and D) *TGFBR1* and *TGFBR2* were knocked out in TMEM2-OE cells, followed by CF mitochondrial stress resistance assays (C) and AUC comparison (D). $n = 8$.

(E) RNA-seq was performed on WT, *TMEM2-OE*, and *TGFBR1-KO TMEM2-OE* fibroblasts. Significantly up- or down-regulated genes (p-adj < 0.05) of the *TMEM2-OE* vs. WT comparison are shown and compared with changes induced by *TGFBR1-KO*. $n = 4$.

Data represented as mean (C and E) or mean ± SEM (D). One-way ANOVA with post hoc Dunnett's test (D).

See also Figures S3 and S4 and Videos S1, S2, and S3.

mitochondrial stress (Figures 3C and 3D; Videos S1, S2, and S3), as well as the use of the chemical inhibitor of TGFBR1, SB431542 (Figures S3C and S3D). To further assess how much of the TMEM2-induced overall transcriptomic changes is due to the TGF-β signaling, the transcriptomes were compared between wild-type, *TMEM2-OE*, and *TGFBR1-KO TMEM2-OE* cells. Indeed, about 64% of significant up-regulation and 54% of significant down-regulation in *TMEM2-OE* cells was reversed by *TGFBR1-KO* (Figures 3E, S3E, and S3F; Table S2). This indicates that activation of the TGF-β signaling pathway plays a major role in driving *TMEM2-OE*-induced transcriptional changes, although other signaling pathways may also contribute to the complicated outcome induced by *TMEM2 OE*. Moreover, this screen generated a list of ECM genes whose KO sensitized cells to mitochondrial stress (Figures S3G–S3I), indicating the possible participation of more ECM-related proteins in maintaining mitochondrial homeostasis. This dataset provides a comprehensive view on how the ECM may impact mitochondria through various pathways.

To our surprise, we did not uncover integrin or HA-signaling pathways in the *TMEM2-OE* CRISPR-KO screen. The signaling role of HA is often mediated by various HABPs, such as CD44 and LYVE1.[16] We formally tested whether these pathways may regulate the TMEM2-mitochondria signaling. As a marker for integrin signaling, FAK phosphorylation was measured, and no significant alterations were observed in *TMEM2-OE* and *TMEM2-KO* cells (Figures S3J–S3N), indicating that integrin activities are not directly affected by TMEM2-induced ECM remodeling. This conclusion is further substantiated by findings in *C. elegans*, where hTMEM2 retained its capacity to robustly induce UPR^{MT} even when *pat-3*, the ortholog of human integrin-β,[37] was knocked down (Figures S3O and S3P), indicating that integrins are not required for hTMEM2-induced mitochondrial stress signaling in *C. elegans*.

To test whether any HABPs may regulate TMEM2-induced mitochondrial remodeling, a targeted CRISPR-KO screen was performed, involving the KO of each individual known HABP in wild-type cells, *TMEM2-KO* cells, and *TMEM2-OE* cells, followed by mitochondrial stress resistance assays (Figures S4A–S4D). None of the examined HABPs were essential for the hyper-sensitivity observed in *TMEM2-OE* cells or for the hyper-resistance in *TMEM2-KO* cells, except for one gene, *P32*

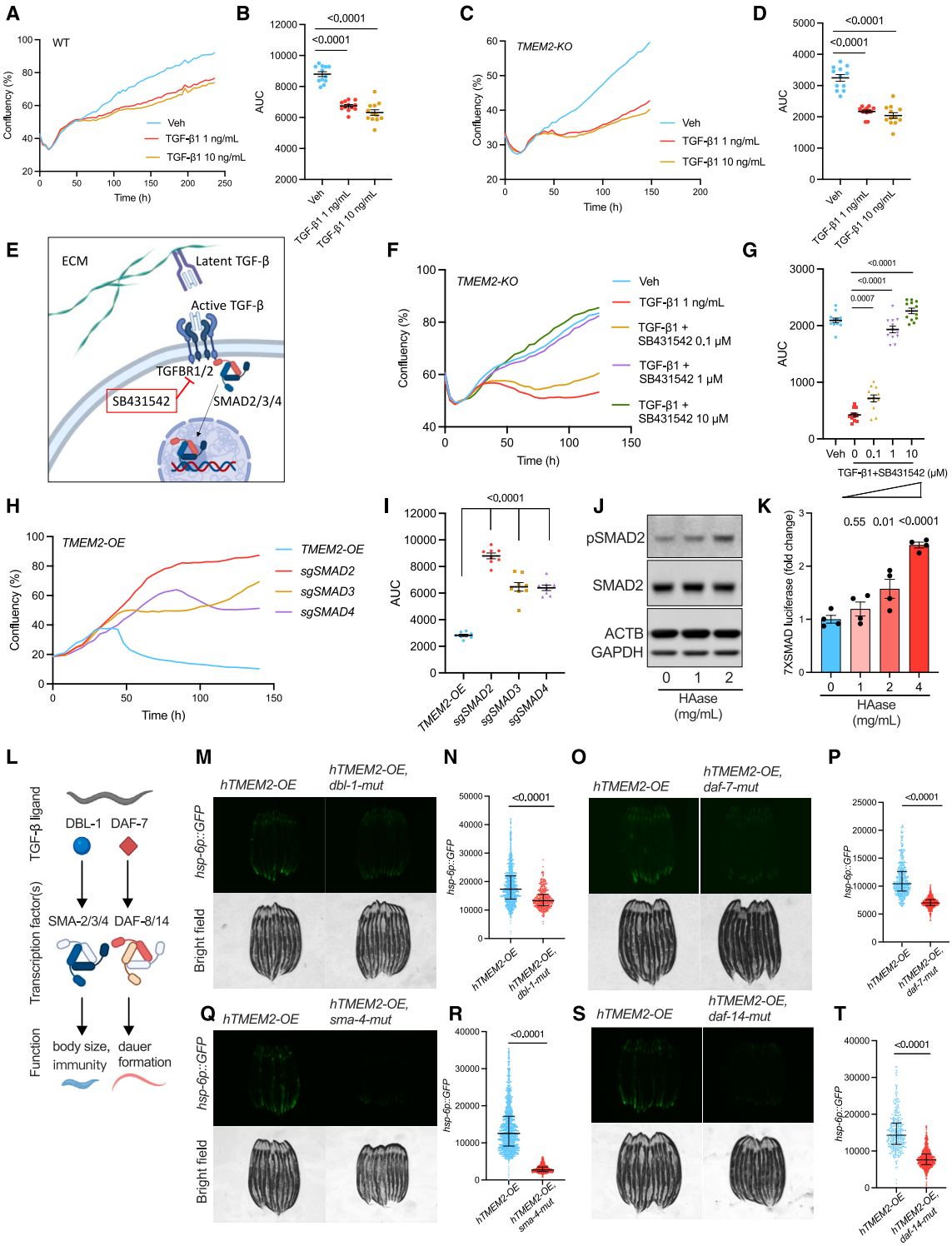

Figure 4. TMEM2 regulates mitochondrial homeostasis via the TGF-β-SMAD signaling pathway

(A–D) Cells of indicated genotypes were treated with TGF-β1 at indicated concentrations for rotenone stress resistance assays using Incucyte (A and C). AUC values were calculated for statistical analyses (B and D). *n* = 12.

(E) Latent TGF-β is stored in the ECM. Upon activation, TGF-β signals via the TGFBR-SMAD pathway.

(F and G) *TMEM2-KO* cells were treated with 1 ng/mL TGF-β1 and indicated doses of SB431542 for rotenone stress resistance assays (F). AUC values were calculated for statistical analyses (G). *n* = 12.

(legend continued on next page)

(Figure S4D). Indeed, *P32-KO* cells were sensitive to multiple mitochondrial stresses (Figures S4E–S4J), indicating that P32 may preserve mitochondrial homeostasis. However, *P32-KO* did not suppress the rotenone-resistance phenotype induced by *TMEM2-KO* (Figures S4I and S4J), raising the possibility that P32 and TMEM2 may operate in parallel pathways. Moreover, P32 is mainly localized within mitochondria (Figure S4K) and is therefore unlikely to directly perceive and interact with HA in the ECM. These insights align with previous studies suggesting that P32 functions as a mitochondrial protein controlling mitochondrial translation.[48]

Taken together, TMEM2-induced HA remodeling in the ECM does not signal through integrins or HABPs to regulate mitochondrial homeostasis but rather activates ECM-associated signaling pathways such as TGF-β.

TMEM2 regulates mitochondrial homeostasis via the TGF-β-SMAD signaling pathway

The TGF-β-SMAD signaling pathways are highly conserved at the molecular and functional level from nematodes to humans, with a well-documented role in regulating organismal development and immune responses.[49] Therefore, we hypothesized that TMEM2-induced ECM remodeling could be sensed by TGF-β, which subsequently signals to mitochondria in both nematodes and human cells via an evolutionarily conserved signaling pathway.

The TGF-β ligand superfamily is made up of over 30 members. To identify which TGF-β ligand regulates mitochondrial homeostasis in response to ECM alterations, we analyzed the transcriptome of BJ fibroblasts. *TGFB1* emerged as the most abundantly expressed TGF-β ligand gene in BJ fibroblast cells, while *TGFB2*, *INHBA*, *BMP1*, *BMP4*, *GDF11*, and *GDF15* exhibited lower expression levels (Figure S5A). If one of these TGF-β ligands was responsible for ECM-mitochondrial communication, exogenous addition of the TGF-β ligand to wild-type or *TMEM2-KO* cells would be predicted to sensitize these cells to mitochondrial stress, thus phenocopying *TMEM2-OE* cells. Consistent with this hypothesis, addition of TGF-β1 sensitized both wild-type and *TMEM2-KO* cells to mitochondrial stress (Figures 4A–4D). Likewise, TGF-β2 mirrored this pattern by sensitizing cells to mitochondrial stress (Figures S5B and S5C). In contrast, BMP4, GDF11, and GDF15 showed little impact on cellular sensitivity to mitochondrial stress (Figures S5D–S5I).

Both TGF-β1 and TGF-β2 signal via the canonical TGFBR1/TGFBR2 receptor complex (Figure 4E).[49] Loss of TGFBR1 function, using the TGFBR1 inhibitor SB431542, effectively suppressed the sensitizing effects of TGF-β1 and TGF-β2 on cellular vulnerability to mitochondrial stress in a dose-dependent manner (Figures 4F, 4G, S5J, and S5K), indicating that TGF-β1 and TGF-β2 signal via the TGFBR to control mitochondrial homeostasis. Downstream of the TGFBR lies the canonical SMAD signaling pathway. Knocking out each member of the SMAD2/3/4 transcription factor complex was sufficient to protect *TMEM2-OE* cells against mitochondrial stress (Figures 4H and 4I). As a complementary approach to test whether hyaluronidase-induced ECM remodeling may activate the SMAD signaling pathway, we treated wild-type cells with exogenous hyaluronidase and found that hyaluronidase treatment was sufficient to activate the SMAD signaling pathway, as assessed by the pSMAD2 western blot (Figures 4J and S5L), and the luciferase activity of a SMAD transcriptional reporter[50] (Figure 4K). Moreover, supplementing HMW HA to wild-type cells suppressed both basal and TGF-β1-induced SMAD-luciferase activities (Figures S5M and S5N). This observation indicates that HMW HA may interfere with the activation of TGF-β and that TMEM2 may digest HMW HA in the ECM to abrogate such inhibition. We also measured the amount of TGF-β1 in conditioned culture media of *TMEM2-OE* cells. Although activated TGF-β1 was not detectable in all conditions (data not shown), latent TGF-β1 was not significantly altered by TMEM2 (Figure S5O), indicating that TMEM2 does not affect the overall production of TGF-β1 but rather its activation. Taken together, TMEM2-induced ECM remodeling signals via the TGF-β-TGFBR-SMAD signaling pathway to regulate mitochondrial homeostasis.

Intrigued by the finding that TGF-β signaling was necessary and sufficient for regulating mitochondrial homeostasis and functions downstream of TMEM2-induced alterations of the ECM, we asked whether TGF-β signaling might be required for the communication between other forms of ECM remodeling and mitochondria. Fibulin-5 (FBLN5) promotes the assembly of continuous elastin polymers and thus regulates the protein fiber organization of the ECM.[51] Consistent with a loss of ECM homeostasis, cells lacking *FBLN5* were sensitive to mitochondrial stress and phenocopied the mitochondrial defects found in *TMEM2-OE* cells (Figures S5P and S5Q). Furthermore, blocking TGF-β signaling with SB431542 improved the resistance of *FBLN5-KO* cells against mitochondrial stress (Figures S5R and S5S), indicating that FBLN5-associated ECM remodeling may also signal via the TGF-β-TGFBR signaling pathway. Therefore, TGF-β may have the capability to perceive diverse forms of ECM perturbations and subsequently employ the canonical TGFBR-SMAD signaling pathway to regulate mitochondrial homeostasis.

(H and I) SMAD2, SMAD3, and SMAD4 were knocked out in *TMEM2-OE* cells. CF-mediated mitochondrial stress assays were performed with Incucyte (H) and AUC calculated for statistical analyses (I). $n = 8$.

(J) WT cells were treated with hyaluronidase (HAase) purified from sheep testes for 24 h. Indicated proteins were measured using western blot.

(K) WT cells expressing a luciferase reporter driven by 7 copies of the SMAD2 DNA-binding motif were treated with HAase for 24 h, followed by the luciferase activity assay. $n = 4$.

(L) Two TGF-β ligands in *C. elegans*, DBL-1, and DAF-7, signal via transcription factors SMA-2/SMA-3/SMA-4 and DAF-8/DAF-14 respectively to regulate animal development and immune responses.

(M–T) *hTMEM2-OE*, *hsp-6p::GFP* reporter animals were crossed with indicated TGF-β pathway mutant strains and GFP measured using fluorescence microscopy (M, O, Q, and S) and a worm sorter (N, P, R, and T). $n = 317–1,197$.

Data represented as mean only (A, C, F, and H), mean ± SEM (B, D, G, I, and K), or median ± interquartile range (N, P, R, and T). One-way ANOVA with post hoc Dunnett's test (B, D, G, I, and K), or Mann-Whitney test (N, P, R, and T).

See also Figure S5.

The TGF-β-SMAD signaling pathway is highly conserved across species. A total of five TGF-β ligands (*dbl-1*, *daf-7*, *unc-129*, *tig-2*, and *tig-3*) have been identified that control developmental and immune responses of *C. elegans* (Figure 4L).[52] To test which of these TGF-β ligands might regulate the hTMEM2-mitochondria pathway in *C. elegans*, existing mutants of these ligands were combined with the *hTMEM2-OE, hsp-6p::GFP* strain. Notably, mutations of either *dbl-1* and *daf-7*, but not *tig-2* or *unc-129*, abrogated the induction of the UPR^{MT} in *hTMEM2-OE* animals (Figures 4M–4P and S5T–S5V).[53] Moreover, *sma-4* (the nematode ortholog of *SMAD4*) and *daf-14* (the nematode ortholog of *SMAD2*) were required for hTMEM2-induced UPR^{MT} (Figures 4Q–4T). The genes *sma-4* and *daf-14* were also required for hTMEM2-induced oxidative stress responses (Figures S5W–S5Z), possibly through modulating mitochondrial homeostasis as well. Therefore, consistent with findings in human cells, the TGF-β signaling pathway also regulates mitochondrial homeostasis in response to *hTMEM2* OE in *C. elegans*.

TMEM2-induced TGF-β signaling induces mitochondrial fission

Based on our observations that TGF-β1 sensitizes cells to mitochondrial stress (Figures 4A–4D), we hypothesized that TGF-β1 might directly induce mitochondrial form and/or functional changes in wild-type cells. Much like *TMEM2-OE* cells, TGF-β1 promoted the accumulation of enlarged mitochondrial puncta, indicative of augmented mitochondrial fragmentation (Figures 5A and 5B). When we assessed mitochondrial function, we found reduced OCR in TGF-β1-treated cells, which was rescued by the TGFBR inhibitor SB431542 (Figure 5C), indicating that the canonical TGF-β1 signaling pathway inhibits mitochondrial respiration. Notably, SB431542 alone also mildly increased the OCR of wild-type cells (Figure 5C), indicating that a low level of TGF-β1 signaling may be constitutively active in repressing mitochondrial functions under basal growth conditions. Moreover, TGF-β1 increased mitochondrial ROS levels, which was also attenuated by SB431542 (Figure 5D). Collectively, these findings indicate that TGF-β1 induces mitochondrial fission and functional deterioration similar to the effects observed with TMEM2-OE.

As demonstrated earlier, the SMAD pathway regulates mitochondrial stress responses in both human cells and nematodes (Figure 4). Therefore, we postulated that TGF-β1 might induce mitochondrial remodeling via the canonical SMAD pathway, potentially by inducing transcriptional alterations in specific mitochondrial genes. To test this hypothesis, RNA-seq analysis was performed on TGF-β1-treated cells. Remarkably, among the multitude of mitochondrial genes examined, several key genes associated with mitochondrial fission were up-regulated in response to TGF-β1, including *DNM1*, *DRP1*, *UCP2*, *MTFP1*, *MTFR1*, *SPIRE1*, *RALA*, and *BNIP3* (Figure 5E; Table S3). Indeed, the mitochondrial fission genes *DNM1*, *MTFR1*, and *RALA* are direct targets of SMAD3 in human embryonic stem cells,[54] indicating that promoting mitochondrial fission may constitute one facet of the TGF-β1-SMAD program. Interestingly, anti-oxidative stress genes, including *SOD2*, *PPARG*, and *PPARGC1A*, were down-regulated by TGF-β1 (Figure 5E), in line with the increased generation of ROS observed in these cells.

To test whether mitochondrial fission plays a causative role in TMEM2-induced mitochondrial functional decline, we treated TMEM2-OE cells with two mitochondrial fission inhibitors, P110 and Mdivi-1. Either inhibitor significantly enhanced the resistance of TMEM2-OE cells to mitochondrial stress (Figures 5F–5I). The mitochondrial morphology was restored by P110 or Mdivi-1 treatment, as indicated by reduced mitochondrial puncta in TMEM2-OE cells (Figures 5J and 5K). Moreover, the functional assessment of mitochondrial respiration in TMEM2-OE cells revealed a significant improvement in response to P110 or Mdivi-1 treatment (Figure 5L). Therefore, the TGF-β-SMAD signaling pathway may directly promote the expression of mitochondrial fission genes to modulate mitochondrial homeostasis, including increasing mitochondrial fission, reducing mitochondrial respiration, and increasing mitochondrial oxidative stress, in TMEM2-OE cells.

TMEM2 promotes immunity through mitochondrial stress signaling

The ECM is an enormous structure that provides support for cells and is a key component of the first line of defense against pathogens in the earliest phases of infection. Furthermore, mitochondrial homeostasis is intimately linked with pathogenesis and many pathogens usurp essential mitochondrial metabolites for their own use.[55] Therefore, an intriguing hypothesis has emerged from our findings that could link changes within the ECM to coordinate mitochondrial form and function to allow cells and organisms to defend against pathogens.

Our transcriptomic analyses revealed that the majority of antiviral response genes, including type I interferon-associated immune genes, were significantly up-regulated in *TMEM2-OE* cells (Figure 6A), which were abrogated by knocking out *TGFBR1* (Figure 6B). Mitochondrial DNA (mtDNA), once released into the cytosol, can potently activate the type I interferon signaling pathway.[56,57] We found that both *TMEM2-OE* and TGF-β1 treatment significantly increased the amount of mtDNA in the cytosol (Figures S6A–S6C). This indicates that TMEM2/TGF-β1-induced mitochondrial stress is associated with reduction of the mitochondrial membrane integrity and moderate release of mtDNA, which may in turn activate the type I interferon defense signaling pathway in mammalian cells.

In their natural habitat, wild *C. elegans* consistently confront the risk of bacterial infection, given their reliance on bacteria as a food source. To investigate whether ECM-remodeling-induced mitochondrial stress responses may enhance the immunity of nematodes, we performed pathogen-resistance assays using two human opportunistic pathogenic bacteria, *S. marcescens* and *E. faecalis*. Interestingly, OE of *hTMEM2* (*sur-5p::hTMEM2*) exhibited a robust resistance to both types of pathogenic bacteria (Figures 6C–6E), but had little effect on the lifespan on non-pathogenic *E. coli* (Figure 6F). Furthermore, restricted expression of TMEM2 to the intestine, the major organ in contact with the pathogenic bacteria due to the dense cuticle surrounding the animal, significantly enhanced animal defense against these pathogens (Figures 6C–6E). *C. elegans* may lack the cyclic GMP-AMP synthase-stimulator of interferon genes (cGAS-STING)

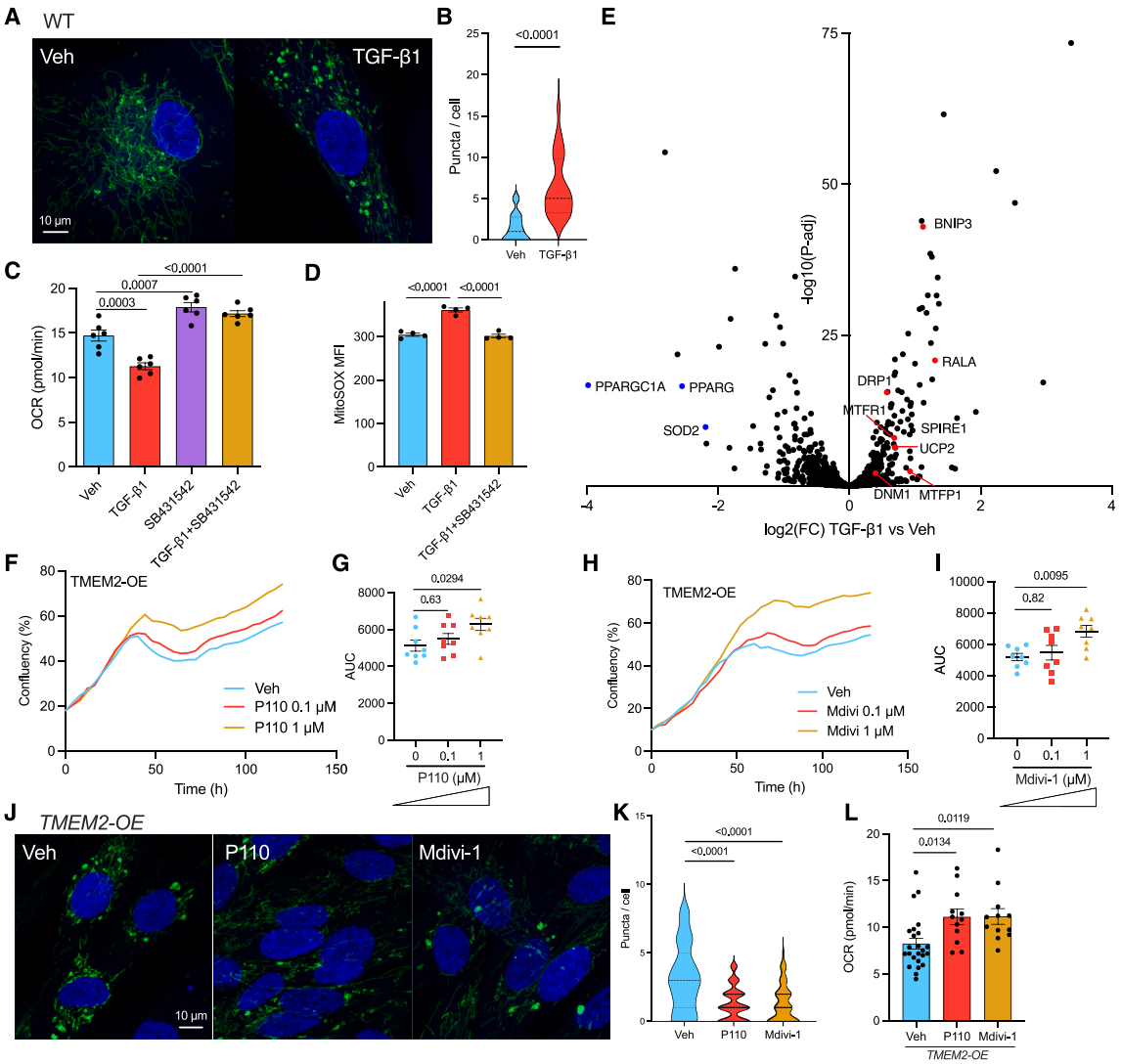

Figure 5. TMEM2-induced TGF-β signaling induces mitochondrial fission

(A and B) WT BJ fibroblasts expressing a mitochondria-GFP reporter were treated with 1 ng/mL TGF-β1 for 24 h. Mitochondria were imaged using an Airyscan confocal microscope (A) and quantified using FIJI (B). *n* = 20–28.

(C and D) WT fibroblasts were treated with TGF-β1 and/or 10 μM SB431542 for 24 h. OCRs were measured by Seahorse (C) and mitochondrial ROS measured by MitoSOX flow cytometry staining (D). *n* = 4–6.

(E) WT fibroblasts were treated with TGF-β1 for 24 h. RNA-seq was performed and mitochondrial genes are selectively shown in this plot. Up-regulated mitochondrial fission genes are highlighted in red. *n* = 4.

(F–I) *TMEM2-OE* fibroblasts were treated with P110 or Mdivi-1 at indicated concentrations for CF mitochondria stress resistance tests (F and H). AUC values were calculated for statistical analyses (G and I). *n* = 8.

(J and K) *TMEM2-OE* fibroblasts expressing a mitochondria-GFP reporter were treated with 1 μM P110 or Mdivi-1 for 24 h, followed by imaging (J) and quantification (K). *n* = 46–160.

(L) *TMEM2-OE* fibroblasts were treated with 1 μM P110 or Mdivi-1 for 24 h, followed by OCR measurement using Seahorse. *n* = 12–24.

Data represented as median ± interquartile range (B and K), mean ± SEM (C, D, G, I, and L), or mean only (F and H). Mann-Whitney test (B), one-way ANOVA with post hoc Tukey's test (C) or post hoc Dunnett's test (D, G, I, and L), or Kruskal-Wallis test with post hoc Dunn's test (K).

pathway and type I interferon responses.[58] Instead, two other mitochondrial-stress-associated responses, namely ATFS-1-mediated UPR^{MT} and SKN-1-mediated oxidative stress response, are key regulators of immunity in nematodes.[32,59] We found that both *atfs-1* and *skn-1* were indispensable for the enhanced defense observed in *hTMEM2-OE* animals (Figures 6G and 6H). Consistent with the *skn-1* requirement, when treated with the antioxidant butylated hydroxyanisole (BHA), both wild-type and *hTMEM2-OE* animals became equally sensitive to *E. faecalis* infection (Figure S6D), further indicating that the oxidative stress signaling plays a key role in mediating *hTMEM2*-enhanced survival. By contrast, *hif-1* was not required

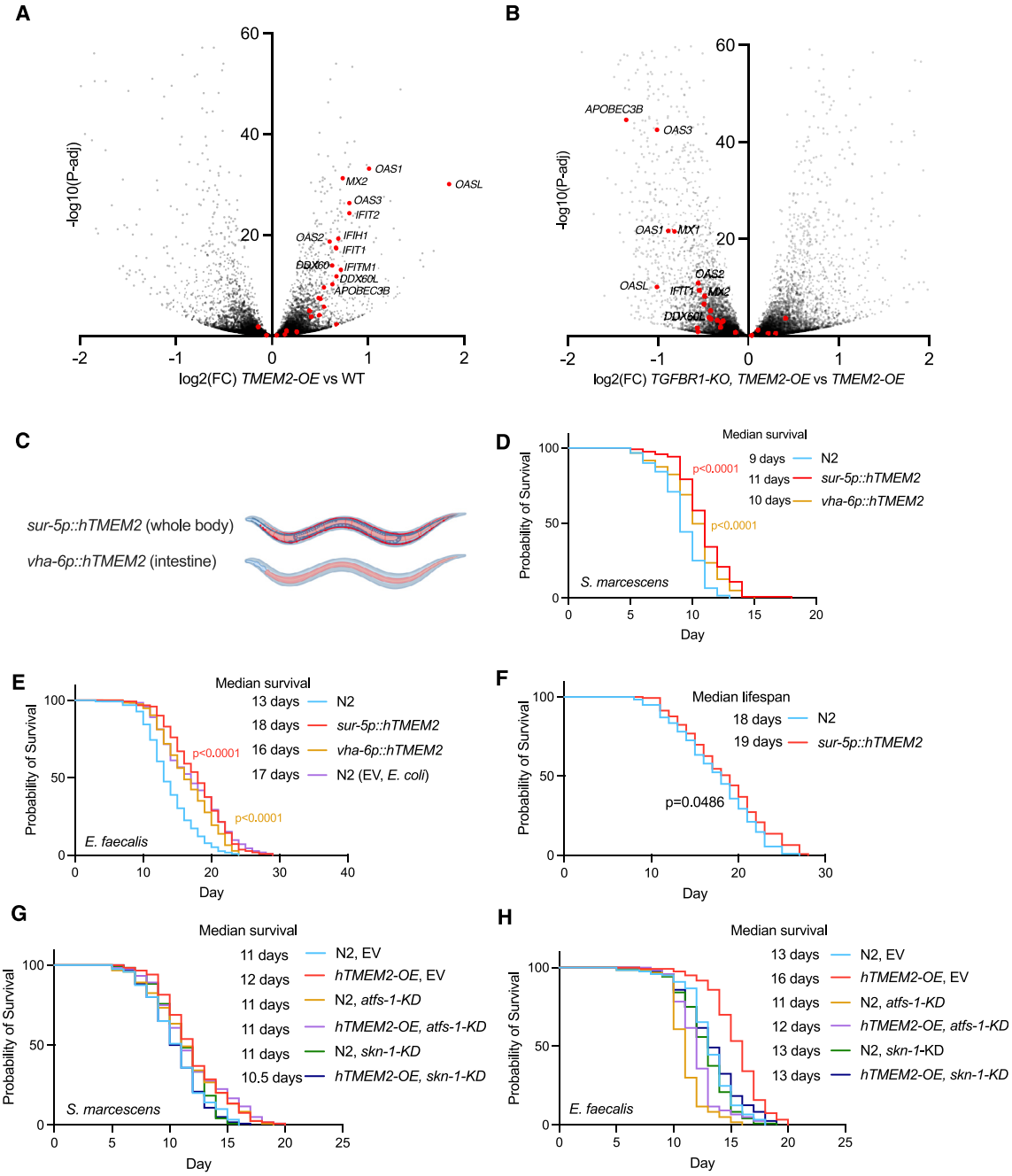

Figure 6. TMEM2 promotes immunity through mitochondrial stress signaling

(A and B) RNA-seq was performed on WT, *TMEM2-OE*, and *TGFBR1-KO TMEM2-OE* fibroblasts. Antiviral response genes (GO: 0051607) were highlighted in red in the *TMEM2-OE* vs. WT comparison (A) and the *TGFBR1-KO TMEM2-OE* vs. *TMEM2-OE* comparison (B). $n = 4$.

(C) Overexpression of *hTMEM2* in the whole body or the intestine of *C. elegans*.

(D and E) Animals of indicated genotypes were grown on EV bacteria until L4 and transferred to *S. marcescens* (D) or *E. faecalis* (E) for pathogen resistance analyses.

(F) Whole-body *hTMEM2-OE* animals or WT animals were grown on EV bacteria for lifespan analyses.

(G and H) Animals of indicated genotypes were grown on indicated RNAi bacteria until L4 and transferred to *S. marcescens* (G) or *E. faecalis* (H), mixed with RNAi bacteria for pathogen resistance analyses.

$N = 120$ for each lifespan group. Log-rank test.

See also Figure S6.

for the enhanced defense in *hTMEM2-OE* animals (Figure S6E). Moreover, using a GFP+ *E. faecalis* strain,[60] we tested whether the improved defense in *hTMEM2-OE* animals was due to more efficient pathogen killing or disease tolerance by the host. Both wild-type and *hTMEM2-OE* animals displayed increased *E. faecalis* colonization with time, with *hTMEM2-OE* animals accumulating slightly more at the later stage (Figures S6F and S6G). Indeed, as a proxy of the feeding efficiency, the pharyngeal pumping rate of infected animals significantly declined with time, but *hTMEM2-OE* animals retained their feeding behavior better (Figure S6H). These observations suggest that *hTMEM2-OE* animals have better tolerance against infection.

Another interesting observation is that hTMEM2 protects animals more efficiently during the *E. faecalis* infection than the *S. marcescens* infection (Figures 6D and 6E), which may result from distinct stress and damage caused by different pathogens. We found that *E. faecalis*, but not *S. marscences*, potently induced UPR^{MT} in *C. elegans* (Figures S6I and S6J). Moreover, *E. faecalis* infection also led to significant reduction of chondroitin in these animals (Figures S6K and S6L), which is consistent with published studies suggesting that *E. faecalis* can generate multiple ECM-remodeling enzymes, including hyaluronidases, to compromise the host barrier.[6,7,61] It is plausible that this TMEM2/ECM-mitochondria immune pathway is more actively involved in defense against ECM-remodeling infections, commonly employed by pathogenic gram-positive bacteria.[14]

Taken together, these findings underscore the notion that hTMEM2-induced ECM remodeling and the associated mitochondrial stress responses may enhance animal immune signaling and offer protection against infections.

DISCUSSION

In our previous work, we found that TMEM2 promotes cellular resistance against the ER stress inducer tunicamycin.[39] However, this protective effect was not mediated through the ER unfolded protein responses (UPR^{ER}).[39] Therefore, we speculated that TMEM2 may signal to regulate other aspects of cellular stress responses rather than directly controlling ER functions. This was tested by various types of stress assays, leading to the discovery that mitochondria are directly regulated by TMEM2 signaling. Specifically, TMEM2-induced ECM remodeling leads to mitochondrial fragmentation and functional declines in both human fibroblasts and *C. elegans*. We eliminated the possibility of HA directly transmitting signals to mitochondria via HABPs. Instead, through a set of genetic screens, we identified the TGF-β signaling pathway as one mediator of TMEM2-induced mitochondrial remodeling by promoting mitochondrial fission. Physiologically, this ECM-mitochondria communicating mechanism may confer specific benefits to animal immunity in a tissue-specific manner.

The most important aspect of this body of work is that it reveals that the ECM has an "alarmin" aspect to it that involves the release of a stored ligand, TGF-β, acting through its receptor and the downstream SMAD signaling complex to alter mitochondrial form and function. It is intriguing to speculate that, during the evolution of eukaryotes, systems originally aimed to protect bacteria before endosymbiosis, such as morphological changes, were handed off to the host cell that alters mitochondrial morphology as a stress response against pathogen infections. As the pathogenic bacteria makes its way through the ECM, alarmins, such as TGF-β, are released to protect the cell from the invading pathogen via remodeling its mitochondria. Indeed, many bacterial pathogens target eukaryotic cells for their mitochondria-rich resources, such as iron, in the case of *Pseudomonas aeruginosa* infection and other siderophore-producing bacterial infections.[62,63] Therefore, besides inducing mitochondrial stress and immune signaling, the ability of mitochondria to divide themselves to create smaller quanta of usable resources by the invading bacteria may limit bacterial growth and avoid more severe mitochondrial damage and cell death, which might be another passive form of early protection from pathogens, and this is mediated by cues from alterations in the ECM.

**In our study we found that alterations of the ECM by either *TMEM2* OE or loss of *FBLN5* resulted in the same TGF-β-mediated signaling and downstream mitochondrial changes. It is interesting to speculate whether all changes of the ECM signal to the cell through TGF-β signaling or whether there will be multiple ECM-derived alarmins. If so, will each alarmin have a distinct set of pathogens that it responds to, thus tailoring the defense modes required for the cell to tolerate and survive the pathogen? Lastly, our work has been focused on fibroblast cells, which are among sentinel cells first encountering pathogens, whereas our *C. elegans* studies became focused on the intestinal cells, one of the few cell types in direct contact with the environment. In the future it will interesting to learn whether other cell types, especially innate immune cells, have the same signaling mechanism and, possibly, more complex systems to signal their ECM changes in a *cis*- and/or *trans*-manner.

In addition to triggering stress responses, mitochondria serve as the central hub of metabolic signaling in cells. Immune activation is often associated with reprogramming of cellular metabolism.[64] For example, pro-inflammatory cell types, such as effector T cells[65,66] and M1 macrophages,[67] exhibit heightened glycolysis, whereas immunosuppressive regulatory T cells[66] and M2 macrophages[68] up-regulate mitochondrial respiration. The TMEM2-induced ECM remodeling results in reduced mitochondrial respiration (Figures 1H, 1I, and 2K), which may also contribute to enhanced immune responses in these cells. Further exploration of TMEM2-induced alterations in cellular metabolism may help unveil another intriguing model wherein ECM remodeling regulates immunity via metabolic rewiring.

Furthermore, this work revealed that a ligand-receptor interaction on the plasma membrane can regulate mitochondrial form and function. Changes to mitochondrial morphology have mainly been driven by intercellular signals, such as mitophagy driven by either PINK1/PARKIN interactions on the mitochondrial surface or DRP1 driving mitochondrial division.[69] Therefore, our findings provide an alternative direction to change mitochondrial function by changing the outside of the cell, the ECM, to drive mitochondrial changes inside of the cell.

The integrity of HA has long been associated with mammalian longevity. The naked mole rat (NMR, *Heterocephalus glaber*) is an extremely long-lived species with a maximal lifespan exceeding 30 years. In comparison, laboratory rats (*Rattus*

norvegicus) with a similar body weight have a lifespan capped at 4 years. One prominent molecular hallmark of NMR cells is the presence of very HMW HA in the ECM, ranging 6,000–12,000 kDa, compared with 500–3,000 kDa in humans and mice.[19] Remarkably, ectopic OE of the NMR HA synthase gene *Has2* (*nmrHas2*) in mice is sufficient to increase HA deposition in multiple tissues, and prolong the lifespans, possibly via reducing inflammation with age.[70] Along with our observations that TMEM2-KO fibroblasts are resistant to mitochondrial and oxidative stress, *nmrHas2*-overexpressing mouse cells also exhibit heightened resistance to H_2O_2-induced oxidative stress. Combining the two studies, a more comprehensive model can be formulated: preserving HA or ECM integrity suppresses immune activation and inflammation to prolong mammalian lifespans, whereas activating ECM-mitochondria signaling can boost immunity across species. An intriguing avenue for future exploration involves manipulating HA integrity in different tissues to achieve an optimal outcome, i.e., extending mammalian lifespans by increasing HA integrity to reduce basal inflammation, while enhancing immune activation efficiency through controlled reduction of HA integrity during infections or vaccinations.

The skin and mucous membranes are the first defense mechanism of the immune system. Breaching this barrier is often the initial step during infection. This breach is facilitated by various ECM-degrading enzymes, including hyaluronidases, collagenases, and elastases, which are secreted by bacteria as key virulent factors.[71] Cell-surface pattern recognition receptors, such as Toll-like receptors (TLRs), are evolutionarily conserved frontline sensors for these microbes through recognizing bacteria-specific structural components, such as lipopolysaccharides and flagellin.[72] On the other hand, immune responses are not exclusively triggered by pathogens. Other forms of tissue damage also elicit immune responses for repair. A common feature between external pathogen invasion and internal tissue damage is the degradation of the ECM. According to our findings, innate immune activation can be achieved, where ECM damage is directly sensed by ECM-bound factors, such as TGF-β, leading to a cascade of mitochondria-based signaling events that activate immune responses coordinated with metabolic remodeling. This pathway operates without the need for specific pattern recognition receptors and hence may have broader implications in tissue damage or other developmentally related ECM remodeling events that are associated with mitochondrial alterations.

Limitations of the study

This research primarily employed genetic approaches to alter HA and other components in the ECM. Further investigation is required to understand the mechanisms of ECM remodeling in specific physiological and pathological contexts, and to test whether different forms of ECM remodeling may trigger distinct stress responses. In particular, whereas TGF-β ligands in mammals are known to be secreted in latent forms and activated upon stimuli in the ECM, it is less clear whether and how ECM remodeling may affect the processing of the TGF-β signaling in *C. elegans*. Moreover, according to our working model, ECM remodeling may induce mitochondrial fission through TGF-β-mediated transcriptional regulations. However, it remains possible that other post-transcriptional and post-translational mechanisms may contribute to the mitochondrial morphological changes we observed. Lastly, we observed that type I interferon response genes were up-regulated by TMEM2 in cultured fibroblasts, prompting the need for more definitive studies about whether ECM remodeling may enhance immune responses in mammals *in vivo*.

STAR★METHODS

Detailed methods are provided in the online version of this paper and include the following:

- KEY RESOURCES TABLE
- RESOURCE AVAILABILITY
  - Lead contact
  - Materials availability
  - Data and code availability
- EXPERIMENTAL MODEL AND STUDY PARTICIPANT DETAILS
  - *C. elegans* maintenance and synchronization
  - Cell culture
- METHOD DETAILS
  - Drug Treatments
  - Western blot
  - ELISA
  - Immunofluorescence staining
  - Incucyte live-cell imaging
  - Seahorse metabolic assays
  - NAD/NADH measurement
  - Correlative light and electron microscopy
  - Flow cytometry
  - RNA-seq library preparation and analysis
  - Fluorescence imaging and quantification in *C. elegans*
  - Alcian blue staining
  - *C. elegans* lifespan measurements
  - BHA treatment
  - Mitochondrial enrichment from fibroblasts
  - Cytosolic mtDNA measurement
  - ATP measurement
  - Lentiviral transduction for expressing vectors in BJ cells
  - CRISPR-KO screen
  - Quantification of mitochondrial features in images using Fiji
- QUANTIFICATION AND STATISTICAL ANALYSIS
- ADDITIONAL RESOURCES
  - Graphics

SUPPLEMENTAL INFORMATION

Supplemental information can be found online at https://doi.org/10.1016/j.cell.2024.05.057.

ACKNOWLEDGMENTS

We thank the members of the Dillin lab and labs of the Immunology and Molecular Medicine division for discussion and technical assistance. This work was supported by grants R01ES021667, R37AG024365, and R01AG082797 from the National Institute of Health and Howard Hughes Medical Institute to A.D., by the Larry L. Hillblom Foundation Postdoctoral Fellowship (2020-A-018-FEL) and the Glenn Foundation for Medical Research Postdoctoral Fellowship to H.Z., by F32AG069388 from the NIA to C.K.T., by T32AG052374 from the NIA to G.G., and by R00AG065200 from the NIA and 2022-A-010-SUP from the Larry L. Hillblom Foundation to R.H.S. This work was also assisted by UC Berkeley core facilities, including the Flow Cytometry Lab, the Sanger DNA Sequencing Facility, the Cell Culture Facility, and the IGI Next Generation Sequencing Core. Thank you to Dr. Danielle Jorgens and Reena Zalpuri at the University of California Berkeley Electron Microscope

Laboratory for advice and assistance in experiment planning, electron microscopy sample preparation, and data collection.

AUTHOR CONTRIBUTIONS

Conceptualization, H.Z. and A.D.; methodology, H.Z., C.K.T., G.G., and R.H.-S.; investigation and formal analysis, H.Z., C.K.T., G.G., L.K.J., H.W., A.M., W.F., S.P., P.H.Y., B.M.W., J.D., P.A.F., and R.H.-S.; writing – original draft, H.Z. and A.D.; writing – review and editing, H.Z., C.K.T., G.G., R.H.-S., and A.D.; visualization, H.Z., J.D., and A.D.; funding acquisition, A.D. and H.Z.; supervision, A.D.

DECLARATION OF INTERESTS

The authors declare no competing interests.

Received: October 17, 2023
Revised: February 22, 2024
Accepted: May 31, 2024
Published: June 27, 2024

REFERENCES

1. Rosales, A.M., and Anseth, K.S. (2016). The design of reversible hydrogels to capture extracellular matrix dynamics. Nat. Rev. Mater. *1*, 15012. https://doi.org/10.1038/natrevmats.2015.12.
2. Chi, S.S., Rattner, J.B., and Matyas, J.R. (2004). Communication between paired chondrocytes in the superficial zone of articular cartilage. J. Anat. *205*, 363–370. https://doi.org/10.1111/j.0021-8782.2004.00350.x.
3. Vink, H., and Duling, B.R. (1996). Identification of distinct luminal domains for macromolecules, erythrocytes, and leukocytes within mammalian capillaries. Circ. Res. *79*, 581–589. https://doi.org/10.1161/01.RES.79.3.581.
4. Hussey, G.S., Keane, T.J., and Badylak, S.F. (2017). The extracellular matrix of the gastrointestinal tract: a regenerative medicine platform. Nat. Rev. Gastroenterol. Hepatol. *14*, 540–552. https://doi.org/10.1038/nrgastro.2017.76.
5. Singh, B., Fleury, C., Jalalvand, F., and Riesbeck, K. (2012). Human pathogens utilize host extracellular matrix proteins laminin and collagen for adhesion and invasion of the host. FEMS Microbiol. Rev. *36*, 1122–1180. https://doi.org/10.1111/j.1574-6976.2012.00340.x.
6. Strateva, T., Atanasova, D., Savov, E., Petrova, G., and Mitov, I. (2016). Incidence of virulence determinants in clinical Enterococcus faecalis and Enterococcus faecium isolates collected in Bulgaria. Braz. J. Infect. Dis. *20*, 127–133. https://doi.org/10.1016/j.bjid.2015.11.011.
7. Rice, L.B., Carias, L., Rudin, S., Vael, C., Goossens, H., Konstabel, C., Klare, I., Nallapareddy, S.R., Huang, W., and Murray, B.E. (2003). A Potential Virulence Gene, *hyl* $_{Efm}$, Predominates in *Enterococcus faecium* of Clinical Origin. J. Infect. DIS. *187*, 508–512. https://doi.org/10.1086/367711.
8. Kobayashi, T., Chanmee, T., and Itano, N. (2020). Hyaluronan: metabolism and function. Biomolecules *10*, 1525. https://doi.org/10.3390/biom10111525.
9. Holmes, M.W.A., Bayliss, M.T., and Muir, H. (1988). Hyaluronic acid in human articular cartilage. Age-related changes in content and size. Biochem. J. *250*, 435–441. https://doi.org/10.1042/bj2500435.
10. Tavianatou, A.G., Caon, I., Franchi, M., Piperigkou, Z., Galesso, D., and Karamanos, N.K. (2019). Hyaluronan: molecular size-dependent signaling and biological functions in inflammation and cancer. FEBS Journal *286*, 2883–2908. https://doi.org/10.1111/febs.14777.
11. Yamamoto, H., Tobisawa, Y., Inubushi, T., Irie, F., Ohyama, C., and Yamaguchi, Y. (2017). A mammalian homolog of the zebrafish transmembrane protein 2 (TMEM2) is the long-sought-after cell-surface hyaluronidase. J. Biol. Chem. *292*, 7304–7313. https://doi.org/10.1074/jbc.M116.770149.
12. De Angelis, J.E., Lagendijk, A.K., Chen, H., Tromp, A., Bower, N.I., Tunny, K.A., Brooks, A.J., Bakkers, J., Francois, M., Yap, A.S., et al. (2017). Tmem2 regulates embryonic Vegf signaling by controlling hyaluronic acid turnover. Dev. Cell *40*, 123–136. https://doi.org/10.1016/j.devcel.2016.12.017.
13. Narita, T., Tobisawa, Y., Bobkov, A., Jackson, M., Ohyama, C., Irie, F., and Yamaguchi, Y. (2023). TMEM2 is a bona fide hyaluronidase possessing intrinsic catalytic activity. J. Biol. Chem. *299*, 105120. https://doi.org/10.1016/j.jbc.2023.105120.
14. Hynes, W.L., and Walton, S.L. (2000). Hyaluronidases of Gram-positive bacteria. FEMS Microbiol. Lett. *183*, 201–207. https://doi.org/10.1111/j.1574-6968.2000.tb08958.x.
15. Dogné, S., and Flamion, B. (2020). Endothelial glycocalyx impairment in disease: Focus on Hyaluronan Shedding. Am. J. Pathol. *190*, 768–780. https://doi.org/10.1016/j.ajpath.2019.11.016.
16. Liang, J., Jiang, D., and Noble, P.W. (2016). Hyaluronan as a therapeutic target in human diseases. Adv. Drug Deliv. Rev. *97*, 186–203. https://doi.org/10.1016/j.addr.2015.10.017.
17. Voelcker, V., Gebhardt, C., Averbeck, M., Saalbach, A., Wolf, V., Weih, F., Sleeman, J., Anderegg, U., and Simon, J. (2008). Hyaluronan fragments induce cytokine and metalloprotease upregulation in human melanoma cells in part by signalling via TLR4. Exp. Dermatol. *17*, 100–107. https://doi.org/10.1111/j.1600-0625.2007.00638.x.
18. Dang, S., Peng, Y., Ye, L., Wang, Y., Qian, Z., Chen, Y., Wang, X., Lin, Y., Zhang, X., Sun, X., et al. (2013). Stimulation of TLR4 by LMW-HA induces metastasis in human papillary thyroid carcinoma through CXCR7. Clin. Dev. Immunol. *2013*, 712561. https://doi.org/10.1155/2013/712561.
19. Tian, X., Azpurua, J., Hine, C., Vaidya, A., Myakishev-Rempel, M., Ablaeva, J., Mao, Z., Nevo, E., Gorbunova, V., and Seluanov, A. (2013). High-molecular-mass hyaluronan mediates the cancer resistance of the naked mole rat. Nature *499*, 346–349. https://doi.org/10.1038/nature12234.
20. Vallet, S.D., Clerc, O., and Ricard-Blum, S. (2021). Glycosaminoglycan–protein interactions: the first draft of the glycosaminoglycan interactome. J. Histochem. Cytochem. *69*, 93–104. https://doi.org/10.1369/0022155420946403.
21. Munger, J.S., Huang, X., Kawakatsu, H., Griffiths, M.J.D., Dalton, S.L., Wu, J., Pittet, J.F., Kaminski, N., Garat, C., Matthay, M.A., et al. (1999). A mechanism for regulating pulmonary inflammation and fibrosis: the integrin αvβ6 binds and activates latent TGF β1. Cell *96*, 319–328. https://doi.org/10.1016/S0092-8674(00)80545-0.
22. Lyons, R.M., Gentry, L.E., Purchio, A.F., and Moses, H.L. (1990). Mechanism of activation of latent recombinant transforming growth factor beta 1 by plasmin. J. Cell Biol. *110*, 1361–1367. https://doi.org/10.1083/jcb.110.4.1361.
23. Massagué, J., and Sheppard, D. (2023). TGF-β signaling in health and disease. Cell *186*, 4007–4037. https://doi.org/10.1016/j.cell.2023.07.036.
24. Shen, K., Pender, C.L., Bar-Ziv, R., Zhang, H., Wickham, K., Willey, E., Durieux, J., Ahmad, Q., and Dillin, A. (2022). Mitochondria as cellular and organismal signaling hubs. Annu. Rev. Cell Dev. Biol. *38*, 179–218. https://doi.org/10.1146/annurev-cellbio-120420-015303.
25. Nargund, A.M., Pellegrino, M.W., Fiorese, C.J., Baker, B.M., and Haynes, C.M. (2012). Mitochondrial import efficiency of ATFS-1 regulates mitochondrial UPR activation. Science *337*, 587–590. https://doi.org/10.1126/science.1223560.
26. Fiorese, C.J., Schulz, A.M., Lin, Y.-F., Rosin, N., Pellegrino, M.W., and Haynes, C.M. (2016). The transcription factor ATF5 mediates a mammalian mitochondrial UPR. Curr. Biol. *26*, 2037–2043. https://doi.org/10.1016/j.cub.2016.06.002.
27. Haynes, C.M., Petrova, K., Benedetti, C., Yang, Y., and Ron, D. (2007). ClpP mediates activation of a mitochondrial unfolded protein response in C. elegans. Dev. Cell *13*, 467–480. https://doi.org/10.1016/j.devcel.2007.07.016.

28. Benedetti, C., Haynes, C.M., Yang, Y., Harding, H.P., and Ron, D. (2006). Ubiquitin-like protein 5 positively regulates chaperone gene expression in the mitochondrial unfolded protein response. Genetics *174*, 229–239. https://doi.org/10.1534/genetics.106.061580.

29. Park, S.K., Tedesco, P.M., and Johnson, T.E. (2009). Oxidative stress and longevity in *Caenorhabditis elegans* as mediated by SKN-1. Aging Cell *8*, 258–269. https://doi.org/10.1111/j.1474-9726.2009.00473.x.

30. Glover-Cutter, K.M., Lin, S., and Blackwell, T.K. (2013). Integration of the unfolded protein and oxidative stress responses through SKN-1/Nrf. PLoS Genet. *9*, e1003701. https://doi.org/10.1371/journal.pgen.1003701.

31. Lima, T., Li, T.Y., Mottis, A., and Auwerx, J. (2022). Pleiotropic effects of mitochondria in aging. Nat Aging *2*, 199–213. https://doi.org/10.1038/s43587-022-00191-2.

32. Pellegrino, M.W., Nargund, A.M., Kirienko, N.V., Gillis, R., Fiorese, C.J., and Haynes, C.M. (2014). Mitochondrial UPR-regulated innate immunity provides resistance to pathogen infection. Nature *516*, 414–417. https://doi.org/10.1038/nature13818.

33. Bárcena, C., Mayoral, P., and Quirós, P.M. (2018). Mitohormesis, an antiaging paradigm. Int. Rev. Cell Mol. Biol. *340*, 35–77. https://doi.org/10.1016/bs.ircmb.2018.05.002.

34. Bonora, M., Bononi, A., De Marchi, E., Giorgi, C., Lebiedzinska, M., Marchi, S., Patergnani, S., Rimessi, A., Suski, J.M., Wojtala, A., et al. (2013). Role of the c subunit of the F $_O$ ATP synthase in mitochondrial permeability transition. Cell Cycle *12*, 674–683. https://doi.org/10.4161/cc.23599.

35. Paradies, G., Ruggiero, F.M., Petrosillo, G., and Quagliariello, E. (1998). Peroxidative damage to cardiac mitochondria: cytochrome oxidase and cardiolipin alterations. FEBS Lett. *424*, 155–158. https://doi.org/10.1016/S0014-5793(98)00161-6.

36. Visavadiya, N.P., Keasey, M.P., Razskazovskiy, V., Banerjee, K., Jia, C., Lovins, C., Wright, G.L., and Hagg, T. (2016). Integrin-FAK signaling rapidly and potently promotes mitochondrial function through STAT3. Cell Commun. Signal. *14*, 32. https://doi.org/10.1186/s12964-016-0157-7.

37. Tharp, K.M., Higuchi-Sanabria, R., Timblin, G.A., Ford, B., Garzon-Coral, C., Schneider, C., Muncie, J.M., Stashko, C., Daniele, J.R., Moore, A.S., et al. (2021). Adhesion-mediated mechanosignaling forces mitohormesis. Cell Metab. *33*, 1322–1341.e13. https://doi.org/10.1016/j.cmet.2021.04.017.

38. Davidson, S., Coles, M., Thomas, T., Kollias, G., Ludewig, B., Turley, S., Brenner, M., and Buckley, C.D. (2021). Fibroblasts as immune regulators in infection, inflammation and cancer. Nat. Rev. Immunol. *21*, 704–717. https://doi.org/10.1038/s41577-021-00540-z.

39. Schinzel, R.T., Higuchi-Sanabria, R., Shalem, O., Moehle, E.A., Webster, B.M., Joe, L., Bar-Ziv, R., Frankino, P.A., Durieux, J., Pender, C., et al. (2019). The hyaluronidase, TMEM2, promotes ER homeostasis and longevity independent of the UPRER. Cell *179*, 1306–1318.e18. https://doi.org/10.1016/j.cell.2019.10.018.

40. Moehle, E.A., Higuchi-Sanabria, R., Tsui, C.K., Homentcovschi, S., Tharp, K.M., Zhang, H., Chi, H., Joe, L., de los Rios Rogers, M., Sahay, A., et al. (2021). Cross-species screening platforms identify EPS-8 as a critical link for mitochondrial stress and actin stabilization. Sci. Adv. *7*, eabj6818. https://doi.org/10.1126/sciadv.abj6818.

41. Cartes-Saavedra, B., Lagos, D., Macuada, J., Arancibia, D., Burté, F., Sjöberg-Herrera, M.K., Andrés, M.E., Horvath, R., Yu-Wai-Man, P., Hajnóczky, G., et al. (2023). *OPA1* disease-causing mutants have domain-specific effects on mitochondrial ultrastructure and fusion. Proc. Natl. Acad. Sci. USA *120*, e2207471120. https://doi.org/10.1073/pnas.2207471120.

42. Kim, H., Lee, J.Y., Park, K.J., Kim, W.-H., and Roh, G.S. (2016). A mitochondrial division inhibitor, Mdivi-1, inhibits mitochondrial fragmentation and attenuates kainic acid-induced hippocampal cell death. BMC Neurosci. *17*, 33. https://doi.org/10.1186/s12868-016-0270-y.

43. Özbek, S., Balasubramanian, P.G., Chiquet-Ehrismann, R., Tucker, R.P., and Adams, J.C. (2010). The evolution of extracellular matrix. Mbo *C 21*, 4300–4305. https://doi.org/10.1091/mbc.e10-03-0251.

44. Yamada, S., Van Die, I., Van Den Eijnden, D.H., Yokota, A., Kitagawa, H., and Sugahara, K. (1999). Demonstration of glycosaminoglycans in *Caenorhabditis elegans*. FEBS Lett. *459*, 327–331. https://doi.org/10.1016/S0014-5793(99)01286-7.

45. Wang, W., Wang, J., and Li, F. (2017). Hyaluronidase and chondroitinase. In Protein Reviews Advances in Experimental Medicine and Biology, M.Z. Atassi, ed. (Springer), pp. 75–87. https://doi.org/10.1007/5584_2016_54.

46. Chatel, A., Hemming, R., Hobert, J., Natowicz, M.R., Triggs-Raine, B., and Merz, D.C. (2010). The C. elegans hyaluronidase: A developmentally significant enzyme with chondroitin-degrading activity at both acidic and neutral pH. Matrix Biol. *29*, 494–502. https://doi.org/10.1016/j.matbio.2010.05.005.

47. Ma, D.K., Vozdek, R., Bhatla, N., and Horvitz, H.R. (2012). CYSL-1 interacts with the O2-sensing hydroxylase EGL-9 to promote H2S-modulated hypoxia-induced behavioral plasticity in C. elegans. Neuron *73*, 925–940. https://doi.org/10.1016/j.neuron.2011.12.037.

48. Yagi, M., Uchiumi, T., Takazaki, S., Okuno, B., Nomura, M., Yoshida, S., Kanki, T., and Kang, D. (2012). p32/gC1qR is indispensable for fetal development and mitochondrial translation: importance of its RNA-binding ability. Nucleic Acids Res. *40*, 9717–9737. https://doi.org/10.1093/nar/gks774.

49. Tominaga, K., and Suzuki, H.I. (2019). TGF-β signaling in cellular senescence and aging-related pathology. Int. J. Mol. Sci. *20*, 5002. https://doi.org/10.3390/ijms20205002.

50. Sarrion-Perdigones, A., Gonzalez, Y., and Venken, K.J.T. (2020). Rapid and efficient synthetic assembly of multiplex luciferase reporter plasmids for the simultaneous monitoring of up to six cellular signaling pathways. Curr. Protoc. Mol. Biol. *131*, e121. https://doi.org/10.1002/cpmb.121.

51. Claus, S., Fischer, J., Mégarbané, H., Mégarbané, A., Jobard, F., Debret, R., Peyrol, S., Saker, S., Devillers, M., Sommer, P., et al. (2008). A p.C217R mutation in fibulin-5 from cutis laxa patients is associated with incomplete extracellular matrix formation in a skin equivalent model. J. Invest. Dermatol. *128*, 1442–1450. https://doi.org/10.1038/sj.jid.5701211.

52. Gumienny, T.L., and Savage-Dunn, C. (2013). TGF-β signaling in C. elegans. WormBook *1–34*, 1–34. https://doi.org/10.1895/wormbook.1.22.2.

53. Xin, N., Durieux, J., Yang, C., Wolff, S., Kim, H.-E., and Dillin, A. (2022). The UPRmt preserves mitochondrial import to extend lifespan. J. Cell Biol. *221*, e202201071. https://doi.org/10.1083/jcb.202201071.

54. Mullen, A.C., Orlando, D.A., Newman, J.J., Lovén, J., Kumar, R.M., Bilodeau, S., Reddy, J., Guenther, M.G., DeKoter, R.P., and Young, R.A. (2011). Master transcription factors determine cell-type-specific responses to TGF-β signaling. Cell *147*, 565–576. https://doi.org/10.1016/j.cell.2011.08.050.

55. Riquelme, S.A., Liimatta, K., Wong Fok Lung, T., Fields, B., Ahn, D., Chen, D., Lozano, C., Sáenz, Y., Uhlemann, A.-C., Kahl, B.C., et al. (2020). Pseudomonas aeruginosa utilizes Host-Derived Itaconate to Redirect Its Metabolism to Promote Biofilm Formation. Cell Metab. *31*, 1091–1106.e6. https://doi.org/10.1016/j.cmet.2020.04.017.

56. White, M.J., McArthur, K., Metcalf, D., Lane, R.M., Cambier, J.C., Herold, M.J., van Delft, M.F., Bedoui, S., Lessene, G., Ritchie, M.E., et al. (2014). Apoptotic caspases suppress mtDNA-induced STING-mediated Type I IFN production. Cell *159*, 1549–1562. https://doi.org/10.1016/j.cell.2014.11.036.

57. Rongvaux, A., Jackson, R., Harman, C.C.D., Li, T., West, A.P., de Zoete, M.R., Wu, Y., Yordy, B., Lakhani, S.A., Kuan, C.-Y., et al. (2014). Apoptotic caspases prevent the induction of Type I interferons by mitochondrial DNA. Cell *159*, 1563–1577. https://doi.org/10.1016/j.cell.2014.11.037.

58. Wu, X., Wu, F.-H., Wang, X., Wang, L., Siedow, J.N., Zhang, W., and Pei, Z.-M. (2014). Molecular evolutionary and structural analysis of the

cytosolic DNA sensor cGAS and STING. Nucleic Acids Res. *42*, 8243–8257. https://doi.org/10.1093/nar/gku569.

59. Papp, D., Csermely, P., and Sőti, C. (2012). A role for SKN-1/Nrf in pathogen resistance and immunosenescence in *Caenorhabditis elegans*. PLoS Pathog. *8*, e1002673. https://doi.org/10.1371/journal.ppat.1002673.
60. Willett, J.L.E., Dale, J.L., Kwiatkowski, L.M., Powers, J.L., Korir, M.L., Kohli, R., Barnes, A.M.T., and Dunny, G.M. (2021). Comparative biofilm assays using Enterococcus faecalis OG1RF identify new determinants of biofilm formation. mBio *12*, e0101121. https://doi.org/10.1128/mBio.01011-21.
61. Steck, N., Hoffmann, M., Sava, I.G., Kim, S.C., Hahne, H., Tonkonogy, S.L., Mair, K., Krueger, D., Pruteanu, M., Shanahan, F., et al. (2011). Enterococcus faecalis metalloprotease compromises epithelial barrier and contributes to intestinal inflammation. Gastroenterology *141*, 959–971. https://doi.org/10.1053/j.gastro.2011.05.035.
62. Kang, D., Kirienko, D.R., Webster, P., Fisher, A.L., and Kirienko, N.V. (2018). Pyoverdine, a siderophore from *Pseudomonas aeruginosa*, translocates into *C. elegans*, removes iron, and activates a distinct host response. Virulence *9*, 804–817. https://doi.org/10.1080/21505594.2018.1449508.
63. Seyoum, Y., Baye, K., and Humblot, C. (2021). Iron homeostasis in host and gut bacteria – a complex interrelationship. Gut Microbes *13*, 1–19. https://doi.org/10.1080/19490976.2021.1874855.
64. Leone, R.D., and Powell, J.D. (2020). Metabolism of immune cells in cancer. Nat. Rev. Cancer *20*, 516–531. https://doi.org/10.1038/s41568-020-0273-y.
65. Wang, R., Dillon, C.P., Shi, L.Z., Milasta, S., Carter, R., Finkelstein, D., McCormick, L.L., Fitzgerald, P., Chi, H., Munger, J., et al. (2011). The transcription factor Myc controls metabolic reprogramming upon T lymphocyte activation. Immunity *35*, 871–882. https://doi.org/10.1016/j.immuni.2011.09.021.
66. Michalek, R.D., Gerriets, V.A., Jacobs, S.R., Macintyre, A.N., MacIver, N.J., Mason, E.F., Sullivan, S.A., Nichols, A.G., and Rathmell, J.C. (2011). Cutting edge: distinct glycolytic and lipid oxidative metabolic programs are essential for effector and regulatory CD4+ T cell subsets. J. Immunol. *186*, 3299–3303. https://doi.org/10.4049/jimmunol.1003613.
67. Freemerman, A.J., Johnson, A.R., Sacks, G.N., Milner, J.J., Kirk, E.L., Troester, M.A., Macintyre, A.N., Goraksha-Hicks, P., Rathmell, J.C., and Makowski, L. (2014). Metabolic reprogramming of macrophages: glucose transporter 1 (GLUT1)-mediated glucose metabolism drives a proinflammatory phenotype. J. Biol. Chem. *289*, 7884–7896. https://doi.org/10.1074/jbc.M113.522037.
68. Vats, D., Mukundan, L., Odegaard, J.I., Zhang, L., Smith, K.L., Morel, C.R., Wagner, R.A., Greaves, D.R., Murray, P.J., and Chawla, A. (2006). Oxidative metabolism and PGC-1β attenuate macrophage-mediated inflammation. Cell Metab. *4*, 13–24. https://doi.org/10.1016/j.cmet.2006.05.011.
69. Chan, D.C. (2020). Mitochondrial dynamics and its involvement in disease. Annu. Rev. Pathol. *15*, 235–259. https://doi.org/10.1146/annurev-pathmechdis-012419-032711.
70. Zhang, Z., Tian, X., Lu, J.Y., Boit, K., Ablaeva, J., Zakusilo, F.T., Emmrich, S., Firsanov, D., Rydkina, E., Biashad, S.A., et al. (2023). Increased hyaluronan by naked mole-rat Has2 improves healthspan in mice. Nature *621*, 196–205. https://doi.org/10.1038/s41586-023-06463-0.
71. Alfano, M., Canducci, F., Nebuloni, M., Clementi, M., Montorsi, F., and Salonia, A. (2016). The interplay of extracellular matrix and microbiome in urothelial bladder cancer. Nat. Rev. Urol. *13*, 77–90. https://doi.org/10.1038/nrurol.2015.292.
72. Kumar, V., and Barrett, J.E. (2022). Toll-like receptors (TLRs) in health and disease: an overview. In Toll-Like Receptors in Health and Disease Handbook of Experimental Pharmacology, V. Kumar, ed. (Springer International Publishing), pp. 1–21. https://doi.org/10.1007/164_2021_568.
73. Bryant, J.D., Lei, Y., VanPortfliet, J.J., Winters, A.D., and West, A.P. (2022). Assessing mitochondrial DNA release into the cytosol and subsequent activation of innate immune-related pathways in mammalian cells. Curr. Protoc. *2*, e372. https://doi.org/10.1002/cpz1.372.
74. Afgan, E., Baker, D., van den Beek, M., Blankenberg, D., Bouvier, D., Čech, M., Chilton, J., Clements, D., Coraor, N., Eberhard, C., et al. (2016). The Galaxy platform for accessible, reproducible and collaborative biomedical analyses: 2016 update. Nucleic Acids Res. *44*, W3–W10. https://doi.org/10.1093/nar/gkw343.
75. The Galaxy Community, Afgan, E., Nekrutenko, A., Grüning, B.A., Blankenberg, D., Goecks, J., Schatz, M.C., Ostrovsky, A.E., Mahmoud, A., and Lonie, A.J. (2022). The Galaxy platform for accessible, reproducible and collaborative biomedical analyses: 2022 update. Nucleic Acids Res. *50*, W345–W351. https://doi.org/10.1093/nar/gkac247.
76. Cary, M., Podshivalova, K., and Kenyon, C. (2020). Application of transcriptional gene modules to analysis of *Caenorhabditis elegans* ' gene expression. G3 (Bethesda) *10*, 3623–3638. https://doi.org/10.1534/g3.120.401270.
77. Schieber, M., and Chandel, N.S. (2014). TOR signaling couples oxygen sensing to lifespan in C. elegans. Cell Rep. *9*, 9–15. https://doi.org/10.1016/j.celrep.2014.08.075.
78. Sanson, K.R., Hanna, R.E., Hegde, M., Donovan, K.F., Strand, C., Sullender, M.E., Vaimberg, E.W., Goodale, A., Root, D.E., Piccioni, F., et al. (2018). Optimized libraries for CRISPR-Cas9 genetic screens with multiple modalities. Nat. Commun. *9*, 5416. https://doi.org/10.1038/s41467-018-07901-8.
79. Tsui, C.K., Twells, N., Doan, E., Woo, J., Khosrojerdi, N., Brooks, J., Kulepa, A., Webster, B., Mahal, L.K., and Dillin, A. (2024). CRISPR screens and lectin microarrays identify novel high mannose N-glycan regulators. Preprint at bioRxiv. https://doi.org/10.1101/2023.10.23.563662.
80. Han, K., Jeng, E.E., Hess, G.T., Morgens, D.W., Li, A., and Bassik, M.C. (2017). Synergistic drug combinations for cancer identified in a CRISPR screen for pairwise genetic interactions. Nat. Biotechnol. *35*, 463–474. https://doi.org/10.1038/nbt.3834.
81. Morgens, D.W., Deans, R.M., Li, A., and Bassik, M.C. (2016). Systematic comparison of CRISPR/Cas9 and RNAi screens for essential genes. Nat. Biotechnol. *34*, 634–636. https://doi.org/10.1038/nbt.3567.

STAR★METHODS

KEY RESOURCES TABLE

REAGENT or RESOURCE	SOURCE	IDENTIFIER
Antibodies		
LAMP1	Cell Signaling Technology	9091S; RRID:AB_2687579
Donkey anti-Rabbit IgG, AF488	Thermo Fisher	A21206; RRID:AB_2535792
TMEM2	Sigma	HPA044889; RRID:AB_10962641
ACTB	Cell Signaling Technology	3700; RRID:AB_2242334
ATP5A	Abcam	ab14748; RRID:AB_301447
GAPDH	Millipore	MAB374; RRID:AB_2107445
p-FAK Tyr925	Cell Signaling Technology	3284; RRID:AB_10831810
p-FAK Tyr397	Cell Signaling Technology	8556; RRID:AB_10891442
p-FAK Tyr576/577	Cell Signaling Technology	3281; RRID:AB_331079
FAK	Cell Signaling Technology	13009; RRID:AB_2798086
P32	Thermo Fisher	PA5-55318; RRID:AB_2638956
H3	Proteintech	17168-1-AP; RRID:AB_2716755
COXIV	Proteintech	66110-1-IG; RRID:AB_2881509
Hyaluronic Acid Binding Protein, Biotinylated	Sigma	385911
Hyaluronic Acid Binding Protein	Sigma	385910
Streptavidin, Alkaline Phosphatase Conjugate	Thermo Fisher	S921
Streptavidin, Alkaline Phosphatase Conjugate	Thermo Fisher	S11223
IRDye 800CW Donkey Anti-Rabbit IgG (H+L)	LI-COR	926-32213; RRID:AB_621848
IRDye 680RD Donkey Anti-Mouse IgG (H+L)	LI-COR	926-68022; RRID:AB_10715072
Bacterial and virus strains		
OP50	CGC	OP50; RRID:WB-STRAIN:WBStrain00041969
HT115	CGC	HT115; RRID:WB-STRAIN:WBStrain00041079
DH5α	Invitrogen	18258012
Stbl3	Thermo Fisher	C7373-03
OG1RF	ATCC	OG1RF; RRID:WB-STRAIN:WBStrain00041967
DB11	CGC	Db11; RRID:WB-STRAIN:WBStrain00041003
OG1RF (GFP+)	Willett et al.[60]	N/A
Chemicals, peptides, and recombinant proteins		
WGA-AF647	Thermo Fisher	W32466
MitoSOX	Thermo Fisher	M36008
MitoTracker Green	Thermo Fisher	M7514
MitoTracker Deep Red	Thermo Fisher	M22426
Alcian Blue 8GX	Polysciences	19175-10
Rotenone	Sigma	R8875-1G
Oligomycin	Sigma	495455-10MG
FCCP	Sigma	C2920-10MG
Antimycin A	Sigma	A8674-25MG
Sodium azide	Sigma	S2002-25G
H_2O_2	Sigma	H1009-5ML
Hyaluronidase	Sigma	H6254-500MG
Brefeldin A	Thermo Fisher	B7450
Cytochalasin D	Thermo Fisher	PHZ1063
Actinomycin D	Sigma	A1410-2MG

(*Continued on next page*)

Continued

REAGENT or RESOURCE	SOURCE	IDENTIFIER
Cycloheximide	Sigma	01810-1G
FUDR	Spectrum Chemical	50-91-9
HMW HA (>950 kDa)	R&D Systems	GLR002
Ultra LMW HA (4-8 kDa)	R&D Systems	GLR003
NAC	Sigma	A9165
SKQ1	Selleck Chemicals	S9729
Chondroitinase ABC	Sigma	C2905-10UN
Recombinant Human TGF-β1	PeproTech	100-21-10UG
Recombinant Human TGF-β2	PeproTech	100-35B
SB431542	Selleck Chemicals	S1067
Recombinant Human BMP-4	PeproTech	120-05
Recombinant Human/Murine/Rat GDF-11	PeproTech	120-11
Recombinant Human GDF-15	PeproTech	120-28C
P110	Selleck Chemicals	S9887
Mdivi-1	APExBio	A4472
Butylated hydroxyanisole (BHA)	Thermo Fisher	235231000
Critical commercial assays		
Firefly Luciferase Glow Assay	Thermo Fisher	16176
CellTiter-Glo® 2.0	Promega	G9242
TGF beta-1 Human/Mouse Uncoated ELISA Kit	Thermo Fisher	88-8350-22
NAD/NADH-Glo™ Assay	Promega	G9071
Seahorse XFe96 FluxPak	Agilent Technologies	102416-100
Deposited data		
Original images	Mendeley	Mendeley Data: https://data.mendeley.com/datasets/5t4fds77m9/draft?a=7c37fe2f-5f74-44cd-8d22-72536b35f474
RNA-seq (TGF-β1 treatment)	SRA	SRA: PRJNA1116727
RNA-seq (TMEM2-OE, TGFBR1-KO)	ArrayExpress	ArrayExpress: E-MTAB-14112
Experimental models: Cell lines		
Human BJ fibroblasts	ATCC	BJ-5ta, CRL-4001; RRID:CVCL_6573
HEK293T	ATCC	CRL-11268; RRID:CVCL_1926
Human BJ fibroblast, pLentiCas9-Blast (WT fibroblast)	Schinzel et al.[39]	N/A
Human BJ fibroblast, pLentiCas9-Blast, pSGR121puro, clonal expansion (TMEM2-KO fibroblast) clone 1	Schinzel et al.[39]	N/A
TMEM2-KO clone 2	This study	N/A
TMEM2-KO clone 3	This study	N/A
Human BJ fibroblast, pLentiCas9-Blast, CMV-TMEM2 (TMEM2-OE fibroblast)	Schinzel et al.[39]	N/A
TMEM2-KO fibroblast, CMV-TMEM2(PAM mutated) (TMEM2-KO + TMEM2-OE)	This study	N/A
TMEM2-OE fibroblast, pMCB320-sgSafe (TMEM2-OE + control sgRNA)	This study	N/A
TMEM2-OE fibroblast, pMCB320-sgTGFBR1	This study	N/A
TMEM2-OE fibroblast, pMCB320-sgTGFBR2	This study	N/A
TMEM2-OE fibroblast, pMCB320-sgSMAD2	This study	N/A
TMEM2-OE fibroblast, pMCB320-sgSMAD3	This study	N/A
TMEM2-OE fibroblast, pMCB320-sgSMAD4	This study	N/A

(*Continued on next page*)

Continued

REAGENT or RESOURCE	SOURCE	IDENTIFIER
WT fibroblast, 7xSMAD_RE::FLuc	This study	N/A
WT fibroblast, pMCB320-sgSafe	This study	N/A
WT fibroblast, pMCB320-sgACAN_1	This study	N/A
WT fibroblast, pMCB320-sgAMBP_1	This study	N/A
WT fibroblast, pMCB320-sgAMBP_2	This study	N/A
WT fibroblast, pMCB320-sgBCAN_1	This study	N/A
WT fibroblast, pMCB320-sgCD44_1	This study	N/A
WT fibroblast, pMCB320-sgCD44_2	This study	N/A
WT fibroblast, pMCB320-sgCEMIP_1	This study	N/A
WT fibroblast, pMCB320-sgCEMIP_2	This study	N/A
WT fibroblast, pMCB320-sgHAPLN1_1	This study	N/A
WT fibroblast, pMCB320-sgHAPLN1_2	This study	N/A
WT fibroblast, pMCB320-sgHAPLN2_1	This study	N/A
WT fibroblast, pMCB320-sgHAPLN2_2	This study	N/A
WT fibroblast, pMCB320-sgHMMR_1	This study	N/A
WT fibroblast, pMCB320-sgHMMR_2	This study	N/A
WT fibroblast, pMCB320-sgITIH1_1	This study	N/A
WT fibroblast, pMCB320-sgITIH1_2	This study	N/A
WT fibroblast, pMCB320-sgITIH2_1	This study	N/A
WT fibroblast, pMCB320-sgITIH2_2	This study	N/A
WT fibroblast, pMCB320-sgLYVE1_1	This study	N/A
WT fibroblast, pMCB320-sgLYVE1_2	This study	N/A
WT fibroblast, pMCB320-sgNCAN_2	This study	N/A
WT fibroblast, pMCB320-sgP32_1	This study	N/A
WT fibroblast, pMCB320-sgP32_2	This study	N/A
WT fibroblast, pMCB320-sgSTAB1_1	This study	N/A
WT fibroblast, pMCB320-sgSTAB1_2	This study	N/A
WT fibroblast, pMCB320-sgSTAB2_1	This study	N/A
WT fibroblast, pMCB320-sgSTAB2_2	This study	N/A
WT fibroblast, pMCB320-sgTLR4_1	This study	N/A
WT fibroblast, pMCB320-sgTLR4_2	This study	N/A
WT fibroblast, pMCB320-sgTNFAIP6_1	This study	N/A
WT fibroblast, pMCB320-sgTNFAIP6_2	This study	N/A
WT fibroblast, pMCB320-sgVCAN_1	This study	N/A
WT fibroblast, pMCB320-sgVCAN_2	This study	N/A
WT fibroblast, pMCB320-sgBCAN_2	This study	N/A
WT fibroblast, pMCB320-sgHABP2_1	This study	N/A
WT fibroblast, pMCB320-sgHABP2_2	This study	N/A
WT fibroblast, pMCB320-sgHAPLN3_1	This study	N/A
WT fibroblast, pMCB320-sgHAPLN3_2	This study	N/A
WT fibroblast, pMCB320-sgHAPLN4_1	This study	N/A
WT fibroblast, pMCB320-sgHAPLN4_2	This study	N/A
WT fibroblast, pMCB320-sgNCAN_1	This study	N/A
WT fibroblast, pMCB320-sgSUSD5_1	This study	N/A
WT fibroblast, pMCB320-sgSUSD5_2	This study	N/A
WT fibroblast, pMCB320-sgITIH3_1	This study	N/A
WT fibroblast, pMCB320-sgITIH3_2	This study	N/A
TMEM2-OE fibroblast, pMCB320-sgSafe	This study	N/A

(*Continued on next page*)

Continued

REAGENT or RESOURCE	SOURCE	IDENTIFIER
TMEM2-OE fibroblast, pMCB320-sgACAN_1	This study	N/A
TMEM2-OE fibroblast, pMCB320-sgAMBP_1	This study	N/A
TMEM2-OE fibroblast, pMCB320-sgAMBP_2	This study	N/A
TMEM2-OE fibroblast, pMCB320-sgBCAN_1	This study	N/A
TMEM2-OE fibroblast, pMCB320-sgCD44_1	This study	N/A
TMEM2-OE fibroblast, pMCB320-sgCD44_2	This study	N/A
TMEM2-OE fibroblast, pMCB320-sgCEMIP_1	This study	N/A
TMEM2-OE fibroblast, pMCB320-sgCEMIP_2	This study	N/A
TMEM2-OE fibroblast, pMCB320-sgHAPLN1_1	This study	N/A
TMEM2-OE fibroblast, pMCB320-sgHAPLN1_2	This study	N/A
TMEM2-OE fibroblast, pMCB320-sgHAPLN2_1	This study	N/A
TMEM2-OE fibroblast, pMCB320-sgHAPLN2_2	This study	N/A
TMEM2-OE fibroblast, pMCB320-sgHMMR_1	This study	N/A
TMEM2-OE fibroblast, pMCB320-sgHMMR_2	This study	N/A
TMEM2-OE fibroblast, pMCB320-sgITIH1_1	This study	N/A
TMEM2-OE fibroblast, pMCB320-sgITIH1_2	This study	N/A
TMEM2-OE fibroblast, pMCB320-sgITIH2_1	This study	N/A
TMEM2-OE fibroblast, pMCB320-sgITIH2_2	This study	N/A
TMEM2-OE fibroblast, pMCB320-sgLYVE1_1	This study	N/A
TMEM2-OE fibroblast, pMCB320-sgLYVE1_2	This study	N/A
TMEM2-OE fibroblast, pMCB320-sgNCAN_2	This study	N/A
TMEM2-OE fibroblast, pMCB320-sgP32_1	This study	N/A
TMEM2-OE fibroblast, pMCB320-sgP32_2	This study	N/A
TMEM2-OE fibroblast, pMCB320-sgSTAB1_1	This study	N/A
TMEM2-OE fibroblast, pMCB320-sgSTAB1_2	This study	N/A
TMEM2-OE fibroblast, pMCB320-sgSTAB2_1	This study	N/A
TMEM2-OE fibroblast, pMCB320-sgSTAB2_2	This study	N/A
TMEM2-OE fibroblast, pMCB320-sgTLR4_1	This study	N/A
TMEM2-OE fibroblast, pMCB320-sgTLR4_2	This study	N/A
TMEM2-OE fibroblast, pMCB320-sgTNFAIP6_1	This study	N/A
TMEM2-OE fibroblast, pMCB320-sgTNFAIP6_2	This study	N/A
TMEM2-OE fibroblast, pMCB320-sgVCAN_1	This study	N/A
TMEM2-OE fibroblast, pMCB320-sgVCAN_2	This study	N/A
TMEM2-OE fibroblast, pMCB320-sgBCAN_2	This study	N/A
TMEM2-OE fibroblast, pMCB320-sgHABP2_1	This study	N/A
TMEM2-OE fibroblast, pMCB320-sgHABP2_2	This study	N/A
TMEM2-OE fibroblast, pMCB320-sgHAPLN3_1	This study	N/A
TMEM2-OE fibroblast, pMCB320-sgHAPLN3_2	This study	N/A
TMEM2-OE fibroblast, pMCB320-sgHAPLN4_1	This study	N/A
TMEM2-OE fibroblast, pMCB320-sgHAPLN4_2	This study	N/A
TMEM2-OE fibroblast, pMCB320-sgNCAN_1	This study	N/A
TMEM2-OE fibroblast, pMCB320-sgSUSD5_1	This study	N/A
TMEM2-OE fibroblast, pMCB320-sgSUSD5_2	This study	N/A
TMEM2-OE fibroblast, pMCB320-sgITIH3_1	This study	N/A
TMEM2-OE fibroblast, pMCB320-sgITIH3_2	This study	N/A
TMEM2-KO fibroblast, pMCB320-sgSafe	This study	N/A
TMEM2-KO fibroblast, pMCB320-sgACAN_1	This study	N/A
TMEM2-KO fibroblast, pMCB320-sgAMBP_1	This study	N/A

(*Continued on next page*)

Continued

REAGENT or RESOURCE	SOURCE	IDENTIFIER
TMEM2-KO fibroblast, pMCB320-sgAMBP_2	This study	N/A
TMEM2-KO fibroblast, pMCB320-sgBCAN_1	This study	N/A
TMEM2-KO fibroblast, pMCB320-sgCD44_1	This study	N/A
TMEM2-KO fibroblast, pMCB320-sgCD44_2	This study	N/A
TMEM2-KO fibroblast, pMCB320-sgCEMIP_1	This study	N/A
TMEM2-KO fibroblast, pMCB320-sgCEMIP_2	This study	N/A
TMEM2-KO fibroblast, pMCB320-sgHAPLN1_1	This study	N/A
TMEM2-KO fibroblast, pMCB320-sgHAPLN1_2	This study	N/A
TMEM2-KO fibroblast, pMCB320-sgHAPLN2_1	This study	N/A
TMEM2-KO fibroblast, pMCB320-sgHAPLN2_2	This study	N/A
TMEM2-KO fibroblast, pMCB320-sgHMMR_1	This study	N/A
TMEM2-KO fibroblast, pMCB320-sgITIH1_1	This study	N/A
TMEM2-KO fibroblast, pMCB320-sgITIH1_2	This study	N/A
TMEM2-KO fibroblast, pMCB320-sgITIH2_1	This study	N/A
TMEM2-KO fibroblast, pMCB320-sgITIH2_2	This study	N/A
TMEM2-KO fibroblast, pMCB320-sgLYVE1_1	This study	N/A
TMEM2-KO fibroblast, pMCB320-sgLYVE1_2	This study	N/A
TMEM2-KO fibroblast, pMCB320-sgNCAN_2	This study	N/A
TMEM2-KO fibroblast, pMCB320-sgP32_1	This study	N/A
TMEM2-KO fibroblast, pMCB320-sgP32_2	This study	N/A
TMEM2-KO fibroblast, pMCB320-sgSTAB1_1	This study	N/A
TMEM2-KO fibroblast, pMCB320-sgSTAB1_2	This study	N/A
TMEM2-KO fibroblast, pMCB320-sgSTAB2_1	This study	N/A
TMEM2-KO fibroblast, pMCB320-sgSTAB2_2	This study	N/A
TMEM2-KO fibroblast, pMCB320-sgTLR4_1	This study	N/A
TMEM2-KO fibroblast, pMCB320-sgTLR4_2	This study	N/A
TMEM2-KO fibroblast, pMCB320-sgTNFAIP6_2	This study	N/A
TMEM2-KO fibroblast, pMCB320-sgVCAN_1	This study	N/A
TMEM2-KO fibroblast, pMCB320-sgVCAN_2	This study	N/A
TMEM2-KO fibroblast, pMCB320-sgBCAN_2	This study	N/A
TMEM2-KO fibroblast, pMCB320-sgHABP2_1	This study	N/A
TMEM2-KO fibroblast, pMCB320-sgHABP2_2	This study	N/A
TMEM2-KO fibroblast, pMCB320-sgHAPLN3_1	This study	N/A
TMEM2-KO fibroblast, pMCB320-sgHAPLN3_2	This study	N/A
TMEM2-KO fibroblast, pMCB320-sgHAPLN4_1	This study	N/A
TMEM2-KO fibroblast, pMCB320-sgHAPLN4_2	This study	N/A
TMEM2-KO fibroblast, pMCB320-sgNCAN_1	This study	N/A
TMEM2-KO fibroblast, pMCB320-sgSUSD5_1	This study	N/A
TMEM2-KO fibroblast, pMCB320-sgSUSD5_2	This study	N/A
WT fibroblast, pMCB320-sgFBLN5	This study	N/A
Experimental models: *C. elegans*		
Bristol (N2) strain as wild type (WT)	CGC	N2; RRID:WB-STRAIN:WBStrain00000001
AGD1952: N2, uthIs485(sur-5p::hTMEM2::unc-54 UTR, myo-2p::tdtomato) strain C4a	Schinzel et al.[39]	N/A
AGD1953: N2, uthIs485(sur-5p::hTMEM2::unc-54 UTR, myo-2p::tdtomato) strain G4e (hTMEM2-OE used in this study)	Schinzel et al.[39]	N/A
AGD1954: N2, uthIs485(sur-5p::hTMEM2::unc-54 UTR, myo-2p::tdtomato) strain E4e	Schinzel et al.[39]	N/A

(*Continued on next page*)

Continued

REAGENT or RESOURCE	SOURCE	IDENTIFIER
AGD3126: zcIs13[hsp-6p::GFP] V (SJ4100 backcrossed 6X)	CGC	SJ4100; RRID:WB-STRAIN:WBStrain00034068
AGD3127: uthEx924 (sur-5p::hTMEM2(R265C, D273N, D286N)::unc-54 UTR) (hTMEM2(ED)-OE)	This study	N/A
AGD3073: sybIs3150(chhy-1p::chhy-1::chhy-1 UTR, myo-2p::mCherry)	This study	N/A
AGD2838: uthSi84[vha-6p::MLS::GFP(65C)::unc-54 3'UTR, cb-unc-119(+)] I; unc-119(ed3) III;	This study	N/A
VC3044: dbl-1(ok3749) V	CGC	VC3044; RRID:WB-STRAIN:WBStrain00037644
CB1372: daf-7(e1372) III	CGC	CB1372; RRID:WB-STRAIN:WBStrain00004310
DR1369: sma-4(e729) III	CGC	DR1369; RRID:WB-STRAIN:WBStrain00006371
DR77: daf-14(m77) IV	CGC	DR77; RRID:WB-STRAIN:WBStrain00006177
CL2166: dvIs19[pAG15(gst-4p::GFP::NLS)] III	CGC	CL2166; RRID:WB-STRAIN:WBStrain00005102
RB1326: unc-129(ok1443) IV	CGC	RB1326; RRID:WB-STRAIN:WBStrain00032025
RB2430: tig-2(ok3336) V	CGC	RB2430; RRID:WB-STRAIN:WBStrain00033105
Oligonucleotides		
MT-D-Loop F, CATAAAGCCTAAATAGCCCACACG	Bryant et al.[73]	N/A
MT-D-Loop R, CCGTGAGTGGTTAATAGGGTGATA	Bryant et al.[73]	N/A
sgRNA sequence (sgSafe)	This paper	N/A
sgRNA sequence (sgTMEM2 clone 2) ATGGAGTTGTTCCTATCGGT	This paper	N/A
sgRNA sequence (sgTMEM2 clone 3) GGCTGAATCCCCGACAGCTA	This paper	N/A
sgRNA sequence (sgTGFBR1) AGAACGTTCGTGGTTCCGTG	This paper	N/A
sgRNA sequence (sgTGFBR2) ACAGTGATCACACTCCATGT	This paper	N/A
sgRNA sequence (sgSMAD2) GTTAGGATCTCGGTGTGTCG	This paper	N/A
sgRNA sequence (sgSMAD3) AGAAGCGCTCCGAATTGGAG	This paper	N/A
sgRNA sequence (sgSMAD4) CAGCCTGCCAGTATACTGGG	This paper	N/A
sgRNA sequence (sgCD44_1) CTTGATGACCTCGTCCCATG	This paper	N/A
sgRNA sequence (sgCD44_2) GCAATATGTGTCATACTGGG	This paper	N/A
sgRNA sequence (sgHMMR_1) GGTATGATGGCTAAGCAAGA	This paper	N/A
sgRNA sequence (sgHMMR_2) AACAACTTATTGAATTGACC	This paper	N/A
sgRNA sequence (sgSTAB2_1) GTTGTCCCCATCGACAATGG	This paper	N/A
sgRNA sequence (sgSTAB2_2) AAATGCCTTCCCAATTACCG	This paper	N/A
sgRNA sequence (sgSTAB1_1) GATGTGTAGGACACCGTTGG	This paper	N/A
sgRNA sequence (sgSTAB1_2) TCTACATCCATGACCCAACG	This paper	N/A
sgRNA sequence (sgLYVE1_1) CAGTGACAGTACCTACTCGG	This paper	N/A

(*Continued on next page*)

Continued

REAGENT or RESOURCE	SOURCE	IDENTIFIER
sgRNA sequence (sgLYVE1_2) TTAGCCCAAACCCCAAGTGT	This paper	N/A
sgRNA sequence (sgHAPLN1_1) GTCGTACAGCTGGTCGAAGG	This paper	N/A
sgRNA sequence (sgHAPLN1_2) AGATTGTAGCGCCCCAGTCG	This paper	N/A
sgRNA sequence (sgCEMIP_1) GATGTGGATGGAATAGACCG	This paper	N/A
sgRNA sequence (sgCEMIP_2) TCTTGCTGTCACGGTCCGAG	This paper	N/A
sgRNA sequence (sgP32_1) ATAATGACAGTCCAACACAA	This paper	N/A
sgRNA sequence (sgP32_2) GGCCCGCTAAACCTCACCGT	This paper	N/A
sgRNA sequence (sgHABP2_1) GCGATGGCTACTCTTACCGA	This paper	N/A
sgRNA sequence (sgHABP2_2) TGGAGGCTTTAAGAGCACGG	This paper	N/A
sgRNA sequence (sgITIH1_1) ACTCGAGTACAATCGTGGAA	This paper	N/A
sgRNA sequence (sgITIH1_2) GAAAGTTAAAGTCCACATTG	This paper	N/A
sgRNA sequence (sgITIH2_1) GTGTGGGTTATCGAACCACA	This paper	N/A
sgRNA sequence (sgITIH2_2) AAAACCATGGAATTGCACAA	This paper	N/A
sgRNA sequence (sgITIH3_1) CACCTTCGAGCTAACCTACG	This paper	N/A
sgRNA sequence (sgITIH3_2) AGGGTAGGTAACACCGTCGA	This paper	N/A
sgRNA sequence (sgAMBP_1) TGCAGAATGGAACATAACCA	This paper	N/A
sgRNA sequence (sgAMBP_2) TAGAGCTTGGCAGTAATGGT	This paper	N/A
sgRNA sequence (sgSUSD5_1) GCAACACTGATGGTCCCTCG	This paper	N/A
sgRNA sequence (sgSUSD5_2) CATGGAGGATTCCCGGACAG	This paper	N/A
sgRNA sequence (sgHAPLN2_1) GGTCATTCACTCTCATCGTG	This paper	N/A
sgRNA sequence (sgHAPLN2_2) GTACCAGTTCAATTACTACG	This paper	N/A
sgRNA sequence (sgHAPLN3_1) TTTGACACGCACACGCCGCG	This paper	N/A
sgRNA sequence (sgHAPLN3_2) CCAGCTTCACTCCATTAAGG	This paper	N/A
sgRNA sequence (sgHAPLN4_1) CGGGTATCGCCATAACGCCG	This paper	N/A
sgRNA sequence (sgHAPLN4_2) AGTCTTGCAGCGTGACGTTG	This paper	N/A
sgRNA sequence (sgACAN_1) TGGCGTCGTAGCGGGATGAG	This paper	N/A
sgRNA sequence (sgACAN_2) GAACCAGCCTATACCCCAGT	This paper	N/A

(*Continued on next page*)

Continued

REAGENT or RESOURCE	SOURCE	IDENTIFIER
sgRNA sequence (sgVCAN_1) TGGGAAGAGAGACAAACTAG sgRNA sequence (sgVCAN_2) GCCAACAAGACCACCCACTG	This paper	N/A
sgRNA sequence (sgNCAN_1) TCATTGGTCAGATCAGCCCA	This paper	N/A
sgRNA sequence (sgNCAN_2) CCCTCGGATAAAGTGGACCA	This paper	N/A
sgRNA sequence (sgBCAN_1) AGGAAAGTCCACTTGACCCG	This paper	N/A
sgRNA sequence (sgBCAN_2) CTTACCTAGGAGCGTCCTAG	This paper	N/A
sgRNA sequence (sgTNFAIP6_1) GCCTATTGCTACAACCCACA	This paper	N/A
sgRNA sequence (sgTNFAIP6_2) TGGGCCCTGGCTTCACAATG	This paper	N/A
sgRNA sequence (sgTLR4_1) ATAAGTCAATAATATCATCG	This paper	N/A
sgRNA sequence (sgTLR4_2) TGTGAGTATGAGAAATGTCA	This paper	N/A
qPCR primer hsp-6-F; GAGATCGTGGAACCGGAAAGGA	This paper	N/A
qPCR primer hsp-6-R; CGGCATTCTTTTCGGCTTCCTT	This paper	N/A
qPCR primer tba-1-F; TCAACACTGCCATCGCCGCC	This paper	N/A
qPCR primer tba-1-R TCCAAGCGAGACCAGGCTTCAG	This paper	N/A
qPCR primer timm-17B.1-F GATTGTTGTCTTGTCGCCATCC	Xin et al.[53]	N/A
qPCR primer timm-17B.1-R ATCACCTTTGGTCCTGAACGG	Xin et al.[53]	N/A
qPCR primer tin-44-F GGGATACGATTAACTCGGACA	Xin et al.[53]	N/A
qPCR primer tin-44-R CTGCATTCGAGCTTTCAACTG	Xin et al.[53]	N/A
qPCR primer tomm-20-F CGGCTACTGCATTTACTTCGA	Xin et al.[53]	N/A
qPCR primer tomm-20-R TCATTGCCTGCTGCAGCTGGA	Xin et al.[53]	N/A
qPCR primer tomm-22-F CGACTTCGTTCAGCAGTTCAT	Xin et al.[53]	N/A
qPCR primer tomm-22-R GCGATCAATGACGTTGTAGATA	Xin et al.[53]	N/A
qPCR primer tomm-40-F AGCTCGTGATGTCTTCCCAAC	Xin et al.[53]	N/A
qPCR primer tomm-40-R TCCAAATCGGTATCCGGTGTT	Xin et al.[53]	N/A
qPCR primer haf-1-F GTTAATCAGACTGCGATCGAGCG	This paper	N/A
qPCR primer haf-1-R CGGGACATATCACATATGGAGAGC	This paper	N/A
qPCR primer atfs-1-F CAATCACCATCAAAATCGGCG	This paper	N/A
qPCR primer atfs-1-R CTTGCTCAATGTCCATTTCGAAC	This paper	N/A

(*Continued on next page*)

Continued

REAGENT or RESOURCE	SOURCE	IDENTIFIER
Recombinant DNA		
pMCB320	Addgene	89359; RRID:Addgene_89359
All sgRNA oligos were cloned into pMCB320 for expressing and packaging using lentivirus.	This paper	N/A
pLentiCMV-moxGFP-TMEM2_neo	This paper	N/A
pFUDW LentiCas9-Blast	Addgene	52962; RRID:Addgene_52962
7xSMAD_RE::FLuc	Addgene	124531; RRID:Addgene_124531
pRHS47 sur-5p::hTMEM2::unc-54 3' UTR	Schinzel et al.[39]	N/A
pRHS54 sur-5p::hTMEM2(R265C, D273N, D286N)::unc-54 3' UTR	Schinzel et al.[39]	N/A
AD18 chhy-1p::chhy-1 (gDNA)::chhy-1 3' UTR	This paper	N/A
pLJM1-3X-HA-EGFP-OMP25	This paper	N/A
Software and algorithms		
FIJI	FIJI (commercial)	https://fiji.sc
Prism 9	GraphPad (commercial)	https://www.graphpad.com
Image Studio Lite	LI-COR (commercial)	https://www.licor.com (discontinued)
FlowJo	FlowJo (commercial)	https://www.flowjo.com
BioRender	BioRender (commercial)	https://www.biorender.com
sgRNA sequence design (CRISPick)	Broad Institute	https://portals.broadinstitute.org/gppx/crispick/public

RESOURCE AVAILABILITY

Lead contact

Further information and requests for resources and reagents should be directed to and will be fulfilled by the lead contact, Dr. Andrew Dillin (dillin@berkeley.edu).

Materials availability

Plasmids, cell lines, and animal lines generated in this study will be made available on request, but we may require a payment and/or a completed Materials Transfer Agreement if there is potential for commercial application.

Data and code availability

All data reported in this paper will be shared by the lead contact upon request. Original images are available at Mendeley (Mendeley Data: https://data.mendeley.com/datasets/5t4fds77m9/draft?a=7c37fe2f-5f74-44cd-8d22-72536b35f474). Original sequencing data files have been deposited at SRA (SRA: PRJNA1116727) or ArrayExpress (ArrayExpress: E-MTAB-14112). Links or accession numbers are also listed in the key resources table. The datasets are publicly available. This paper does not report original code. Any additional information required to reanalyze the data reported in this work paper is available from the lead contact upon request.

EXPERIMENTAL MODEL AND STUDY PARTICIPANT DETAILS

C. elegans maintenance and synchronization

All utilized strains are variations of N2 (RRID:WB-STRAIN:WBStrain00000001) sourced from the Caenorhabditis Genetics Center. Hermaphroditic worms are used for all experiments shown in the paper. The worms are grown on NGM agar dishes with OP50 *E. coli* bacteria (RRID:WB-STRAIN:WBStrain00041969) at a temperature of 15 °C for stock maintenance. For experimentation, worms are grown on RNAi plates (NGM plates with 1 mM IPTG, 100 mg/mL carbenicillin, and 10 mg/mL tetracycline) at 20 °C unless otherwise specified. Worm synchronization is achieved through bleaching utilizing a standard bleaching solution (1.5% sodium hypochlorite, 0.65 M KOH) until all remains are decomposed, leaving only eggs behind. Subsequently, the eggs undergo three washes with M9 solution and plated on RNAi plates seeded with experimental bacteria. All worms utilized for experimentation are fed with HT115 *E. coli* bacteria (RRID:WB-STRAIN:WBStrain00041079) containing either empty vector (EV, pL4440) plasmids or pL4440 plasmids that express double-stranded RNA incorporating the sequence of the target gene. All RNAi vectors were obtained from the Vidal library or the Ahringer library and underwent sequence verification.

Cell culture

Immortalized human foreskin fibroblast cell line was obtained from ATCC (BJ-5ta, CRL-4001; RRID:CVCL_6573), referred to as wild-type BJ fibroblasts. 293T cells (CRL-11268; RRID:CVCL_1926) were obtained from the UC Berkeley Cell Culture Facility. The identity of cell lines were validated through their STR profiling by UC Berkeley DNA Sequencing Facility. Mycoplasma negative status was confirmed by PCR Detection Kit. These cells were cultured in a humidified incubator at 37 °C with 95% air and 5% CO_2 on culture dishes (Corning). The culture medium consisted of DMEM, 10% Fetal Bovine Serum (FBS), 1% Glutamax, 1% Non-Essential Amino Acids (NEAA), and 1% Penicillin/Streptomycin. Upon reaching 90% of confluency, cells were PBS-washed, trypsinized, and then split at the ratio of 1:6 (BJ cells) to 1:16 (293T cells). For long-term storage, cells were frozen in liquid nitrogen with freezing media (FBS + 10% DMSO). Cells were used for up to 10 passages before a new aliquot was thawed.

METHOD DETAILS

Drug Treatments

Rotenone (R8875, Sigma) was added to complete culture media at the concentration of 600 ng/mL (1.52 μM) to cells for mitochondrial stress resistance assays and the CRISPR-KO screening. For treating cells with CF media, complete culture media were aspirated and replaced with pre-warmed glucose-free DMEM media (11966025, Gibco) supplemented with FBS, Glutamax, NEAA, and antibiotics. For Seahorse assays, 10 μM oligomycin (495455, Sigma), 50 μM FCCP (C2920, Sigma), 2.5 μM rotenone, 2.5 μM antimycin A (A8674, Sigma), and 40 mM sodium azide (S2002, Sigma) were used. Natural sheep hyaluronidase (H6254) was added to cells at the concentration of 2 mg/mL. TGF-β1 (1 ng/mL, 100-21, PeproTech), TGF-β2 (1 ng/mL, 100-35B, PeproTech), BMP4 (120-05, PeproTech), GDF11 (120-11, PeproTech), GDF15 (120-28C, PeproTech), P110 (1 μM, S9887, Selleck) were dissolved in PBS and added at otherwise indicated concentrations. SB431542 (10 μM, S1067, Selleck), Mdivi-1 (1 μM, A4472, APExBIO), brefeldin A (100 nM, B7450, Thermo Fisher), cytochalasin D (300 nM, PHZ1063, Thermo Fisher), actinomycin D (10 nM, A1410, Sigma), cycloheximide (5 μM, C7698, Sigma) were dissolved in DMSO and added at otherwise indicated concentrations.

Western blot

Cells were lysed with ice-cold RIPA lysis buffer containing proteinase inhibitors (78439, Thermo Fisher) and phosphatase inhibitors (P5726, Sigma). After centrifuging to remove debris, the protein concentration in the resulting supernatant was determined using the Pierce Rapid Gold BCA Assay (A53225, Thermo Fisher). The supernatant was then mixed with the Reducing Laemmli Sample Buffer and heated at 95 °C for 5 minutes. Subsequently, 10-20 μg of proteins were loaded onto a NuPAGE Novex 4%–12% Bis-Tris gradient gel (NP0336BOX, Thermo Fisher) and separated with MOPS running buffer (NP0001, Thermo Fisher). The separated proteins were later transferred onto a PVDF membrane (Merck Millipore, IPFL00010) and blocked with Li-Cor Intercept (TBS) Blocking Buffer (927-60001, Li-Cor). The membranes were then incubated with primary antibodies diluted in the Blocking Buffer overnight, followed by secondary antibodies dissolved in the Blocking Buffer with 0.01% SDS for imaging using the Odyssey CLx Imaging System. Data analysis was performed using Image Studio Lite or Fiji.

ELISA

For HA ELISA, the ELISA plate (675061, Greiner Bio-One) was coated with 8 μg/ml HABP (385910, Sigma) in the bicarbonate/carbonate coating buffer at 4 °C overnight. After three washes with PBS, the plate was blocked with 1% BSA in PBS at 37 °C for 1 hour, followed with 3 times of PBS washes. The HA standard (HMW HA, GLR002, R&D Systems) was serially diluted in PBS from 3000 ng/mL to 4 ng/mL. Conditioned cell culture media or cell lysate samples were added to the plate without dilution. The plate with samples were incubated at room temperature for 2 hours. After sample incubation, the plate was washed 6 times with PBS-0.05% Tween 20 followed with detection antibody incubation (1 μg/mL HABP-biotin in PBS-0.05% Tween 20, 385911, Sigma) at 37 °C for 1 hour. After 6 times of washing with PBS-0.05% Tween 20, alkaline phosphatase- (AP-) conjugated streptavidin (S921, Thermo Fisher) was diluted in PBS-0.05% Tween 20 to 1 μg/mL and added to the plate for incubation at 37 °C for 1 hour. After 5 washes with PBS-0.05% Tween 20 and once with PBS, the PNPP substrate (37620, Thermo Fisher) dissolved in the pNPP buffer was added for 20–30 minutes. The absorbance was measured at 405 nm by a plate reader. The protein levels of the cell lysate were quantified using the BCA assay for the normalization purpose.

To isolate HA from cell lysates, cells were grown in 12-well plates and washed twice with PBS. The lysis buffer (200 μg/mL proteinase K diluted in PBS) was added at 100 μL/well to digest cells and release HA. The plate with the lysis buffer was first incubated at 37 °C for 30 minutes to detach cells. Then the lysate was transferred to PCR tubes and incubated at 60 °C for 1 hour and 95 °C for 15 minutes to finish the lysis.

To detect TGF-β1 in culture media with cells grown to 80%-90% confluency, the Human/Mouse TGF beta 1 ELISA kit (88-8350, Thermo Fisher) was used according to manufacturer's protocol. The BCA assay was used to quantify cell amount for normalization.

Immunofluorescence staining

Cells were grown on chambered cell culture slides (229168, Celltreat) to reach the confluency of 60%. Live cells were stained with MitoTracker Deep Red (100 nM, M22426, Thermo Fisher) in culture media at 37 °C for 30 minutes. After washing with fresh culture

media, cells were fixed in pre-warmed 3.7% paraformaldehyde (PFA) dissolved in culture media at 37 °C for 10 minutes. After washing once with PBS, fixed cells were permeabilized with ice-cold acetone at 4 °C for 5 min and rinsed multiple times with PBS. Cells were then incubated with an anti-LAMP1 antibody (1:200, D2D11, Cell Signaling Technology) in PBS-1% BSA at 4 °C overnight and then a secondary antibody (1:1000, A21206, Thermo Fisher) in PBS-1% BSA at room temperature for 1 hour. After several times of washing with PBS and once with H_2O, slides were mounted with the VECTASHIELD Vibrance Antifade Mounting Medium with DAPI (H-1800-2, Vector Laboratories) and imaged using an Airyscan super-resolution confocal microscope (Axio Observer, Zeiss).

For WGA staining, cells were fixed with 3.7% PFA at 37 °C for 10 minutes followed by washing with PBS once. WGA-AF647 (W32466, Thermo Fisher) was added at the concentration of 25 μg/mL in PBS for staining the plasma membrane at room temperature for 15 minutes. After washing with PBS and H_2O, slides were mounted with mounting media with DAPI and imaged using a Leica fluorescence microscope (THUNDER Imager, Leica).

Incucyte live-cell imaging

To measure cellular growth in both basal and stress conditions, cells were grown in the Incucyte Live-Cell Analysis System (Incucyte S3), starting at a confluency of 40%. Phase contrast images were acquired at four distinct locations in each well every four hours for four days or longer. The integrated Incucyte software was employed to compute the rise in cellular confluency, serving as an indicator of cellular growth and fitness. For statistical analyses, each imaging region was considered an individual data point.

Seahorse metabolic assays

Measurement of OCR and ECAR was achieved using a Seahorse Extracellular Flux Analyzer (XFe96) according to the manufacturer's protocol. In brief, cells were seeded in a Seahorse XFe96 Cell Culture Microplate (34222, Agilent) and grown to 60-70% confluency at the time of measurement. Agilent Seahorse Extracellular Flux Assay Kits were used for OCR and ECAR measurements. Initially, probes were hydrated in water in a non-CO_2 37 °C incubator overnight, followed by a 1-hour incubation with pre-warmed calibrant. The Seahorse XF DMEM medium (103575-100, Agilent) supplemented with 4.5g/L glucose, 1 mM sodium pyruvate, Glutamax, NEAA, and antibiotics (but excluding FBS) were substituted for regular culture media 1 hour prior to measurement in a 37 °C CO_2-free incubator. Mitochondrial electron transport chain inhibitors were loaded to the probe cartridge. After probes were calibrated in the calibrant buffer, the cell culture plate was loaded for OCR and ECAR measurements.

To measure the OCR of worms, electron transport chain inhibitors were intentionally omitted due to their limited effectiveness in inhibiting live worms. Consequently, only basal OCR was quantified. Specifically, ten worms were introduced to each well, suspended in 150 μL of M9 buffer. The measurement was performed at 20 °C.

NAD/NADH measurement

To measure cellular NAD^+ and NADH, the NAD/NADH-Glo™ Assay Kit (G9071, Promega) was used according to the manufacturer's protocol. In short, cells cultured in a 96-well plate were lysed in the base solution + 1% DTAB lysis buffer and split into two halves for NAD^+ and NADH measurements separately. The ratio of NAD/NADH was calculated using luminescence signal values and normalized to the control group.

Correlative light and electron microscopy

Cells were grown on gridded 35 mm glass-bottom dishes (#P35G-1.5-14-C-GRD, MatTek) to reach 60-80% of confluency and fixed with fixative media (3.7% electron microscopy grade PFA dissolved in culture media) for 30 minutes at room temperature. All fluorescence microscopy images were obtained in the PFA containing media using a fluorescence microscope (Zeiss Axio Observer). Cells were then stored in 2% glutaraldehyde and 2% PFA in 1x PBS at 4 °C.

For embedding, samples were rinsed three times with 1x PBS (5 min each time, room temperature) and immersed in 1% osmium tetroxide with 1.6% potassium ferricyanide in 1x PBS for 30 minutes. Samples were then briefly washed with distilled water and subjected to an ascending ethanol gradient followed by pure ethanol. Samples were progressively infiltrated (using ethanol as the solvent) with Epon resin (EMS, Hatfield) and polymerized at 60 °C for 24-48 hours. Care was taken to ensure that only a thin amount of resin remained within the glass bottom dishes, optimizing the chances for a successful separation of the glass coverslip. Following polymerization, the glass coverslips were removed using ultra-thin Personna razor blades (EMS, Hatfield). Based on the fluorescence imaging result, regions of interest, identified by the gridded alpha-numerical labeling, were carefully excised and trimmed. The trimmed resin blocks were mounted on a large blank resin block using cyanoacrylate glue for sectioning. Serial thin sections of 80 nm thickness were cut using a Leica UC6 ultramicrotome (Leica) from the surface of the block until approximately 4-5 microns in to ensure complete capture of the cell volumes. Section-ribbons were then collected sequentially onto formvar-coated slot grids. The grids were post-stained with 2% uranyl acetate followed by Reynold's lead citrate, for 5 minutes each. The sections were imaged using a FEI Tecnai 12 120kV TEM (FEI, Hillsboro) and data recorded using a Gatan Rio 16 CMOS camera with Gatan Microscopy Suite software (Gatan).

Flow cytometry

Cells were stained with 5 μM MitoSOX (M36008, Thermo Fisher) or 150 nM MitoTracker Green (M7514, Thermo Fisher) in culture media for 20 minutes at 37 °C. After washing and trypsinization, cells were suspended in ice-cold PBS-0.1% BSA-2 mM EDTA

and analyzed using an Attune Flow Cytometer (Thermo Fisher). A minimum of 5,000 events were acquired for each sample. Data were analyzed using FlowJo 10.

RNA-seq library preparation and analysis

RNA was purified using an RNeasy Mini Kit (74106, Qiagen) and stored at -80 °C. Four biological replications were included for each treatment. For Figure 5E, RNA-Seq library preparation was performed using Roche products, KAPA mRNA HyperPrep Kit, and KAPA Unique Dual Index Adapters. NanoDrop and Qubit instruments (Thermo Fisher) were used to measure nucleic acid concentrations. Agilent BioAnalyzer was used to determine the quality of pre-library total RNA and the library. Single direction sequencing was performed using an Illumina NovaSeq, mode S1, SR100 at the Vincent J. Coates Genomic Sequencing Core at University of California, Berkeley. For Figures 3E, 6A/B, and S4E/F, RNASeq library preparation was performed using TruSeq RNA Library Prep kit and Adapter sequences by Azenta. Paired end sequencing was performed on the Illumina NovaSeqX instrument by Azenta.

RNA-Seq analysis was performed by uploading.fastq files to the Galaxy web platform, using the public server at usegalaxy.org. and human FASTA reference transcriptome Homo_sapiens.GRCh38.cdna.all.fa, downloaded from ensembl. Tools included Kallisto Quant v0.46.2+galaxy and DESeq2, v2.11.40.7+galaxy2.[74,75]

For Figures S3A and S7A, published datasets were obtained for targeted re-analyses.[39]

For Figure S3A, the free online platform of the scalar projection method was used to compare the gene fold-changes of the RNA-seq experiment to the reference module-definition matrix.[76] https://kpodshivalova.shinyapps.io/module_activity_sve/.

The antiviral response gene list was obtained from GO0051607.

Fluorescence imaging and quantification in *C. elegans*

To measure the expression of fluorescence reporters in *C. elegans*, animals were randomly picked from a population under white light. They were immobilized in 100 mM sodium azide and positioned on an NGM plate. Immobilized worms were imaged using a Leica M250FA automated fluorescence stereomicroscope equipped with a Hamamatsu ORCA-ER camera. To quantify the expression of these fluorescence reporters, the remaining population were washed off and run through a worm sorter (350-5000-000, Union Biometrica). All fluorescence values obtained from the worm sorter were normalized to extinction values (EXT, a measure of optical density as an indicator of worm size).

To image mitochondrial reporter animals (vha-6p::MLS::GFP(65C)::unc-54 3'UTR), animals were moderately immobilized in 10 mM sodium azide on a glass slide and immediately imaged using an Airyscan super-resolution confocal microscope with Z stacks.

Alcian blue staining

The amount of GAGs significantly changes during development of *C. elegans*. To achieve a tight synchronization of the population, eggs were hatched in M9 solution and L1 worms were arrested at 20 °C overnight. Synchronized L1 animals were transferred onto EV bacteria and grown for 46 hours at 20 °C to reach the L4 stage. Animals were fixed and permeabilized with ice-cold methanol for 2 minutes and then ice-cold acetone for 4 minutes. After washing with M9, animals were stained with 1% (w/v) Alcian blue dissolved in 3% (v/v) acetic acid at room temperature overnight with gentle mixing. Animals were washed with 3% acetic acid for 3-4 times or until no more stain was evident in the rinse buffer. Animals were transferred to a glass slide and images were taken using a Revolve microscope equipped with a color sensor (Echo). As a positive control for degradation of GAGs, fixed N2 animals were treated with 0.1 U/mL Chondroitinase ABC (C2905, Sigma) in its working buffer (50 mM Tris-HCl pH 8.0, 60 mM sodium acetate, 0.01% BSA, 10 mM EDTA) at 37 °C for 4 hours. In the *E. faecalis* assay, larvae animals showed a severe growth defect on 100% *E. faecalis*, which could be resolved by mixing with EV *E. coli* bacteria at the 9:1 (*E. faecalis*: *E. coli*) ratio.

Image analysis was conducted using the Fiji software. The color channels were split and the red channel images were chosen as they most closely reflected the intensity of the blue color. The average intensity of the background area of the image was measured first. Then the hindgut region of every worm in the image was measured using a consistent rectangular measuring tool. The final values (units) was obtained by subtracting the average background intensity from the average intensity of the worm body region.

C. elegans lifespan measurements

Lifespan assessments were carried out on NGM agar plates containing RNAi bacteria. Animals were synchronized through bleaching and subsequently grown to day 1 adulthood at 20°C. Adult worms were transferred every two days to fresh RNAi plates until offspring were no longer visible (approximately 7 days). A total of 120 animals were monitored for mortality at intervals of 1-2 days until all of them had been assessed. Animals experiencing bagging, vulval explosions, or other age-unrelated deaths were excluded from the statistical analysis.

For lifespan assays with pathogenic bacteria, worms were grown on RNAi bacteria until the L4 stage and transferred to plates with pathogenic bacteria. *S. marcescens* (DB11; RRID:WB-STRAIN:WBStrain00041003) was grown on NGM agar plates and *E. faecalis* (OG1RF; RRID:WB-STRAIN:WBStrain00041967) was grown on BHI agar plates. For pathogenic bacteria together with RNAi bacteria, 10 μL DB11 culture was mixed with 190 μL RNAi bacteria and 1 mM IPTG for each 10 mm NGM plate, and 10 μL OG1RF culture was mixed with 10 μL RNAi bacteria, 80 μL LB liquid media, and 1 mM IPTG for each 10 mm BHI plate. Plated bacteria were grown at room temperature overnight before using. Each pathogenic bacterial plate was spotted with 100 μL of 10 mg/mL FUDR (50-91-9, Spectrum Chemical).

BHA treatment

The BHA treatment protocol was adapted from the published method.[77] In short, BHA was dissolved in ethanol (1 M stock) and added to autoclaved RNAi or BHI media at the 1 mM working concentration. Bacteria were plated on cooled media and grown at room temperature overnight. Eggs were hatched on EV plates and grown to the L4 stage (2 days on vehicle EV plates and 3 days on BHA EV plates), then transferred to *E. faecalis* BHI plates to start the lifespan measurement.

Mitochondrial enrichment from fibroblasts

BJ fibroblasts (10-15 million) were harvested and washed once with ice-cold PBS. The cell pellet was resuspended in 1 mL hypotonic buffer (0.5X of the isotonic concentration, 17.5 mM Tris-HCl pH 7.8, 12.5 mM NaCl, 2.5 mM $MgCl_2$) with protease inhibitors and swell for 5-10 minutes on ice. Then the cell suspension was homogenized for 10-15 strokes using a tight fit Dounce homogenizer. 55 μL of Hypertonic buffer (10X of the isotonic concentration, 0.35 M Tris-HCl pH 7.8, 0.25 M NaCl, 50 mM $MgCl_2$) was added to stop the lysis. The homogenate was centrifuged at 1200 g for 3 minutes at 4 °C to pellet unbroken cells, debris, and nuclei. The supernatant that contains mitochondria was collected and centrifuged again at 1200 g for 3 minutes to eliminate heavy contaminants. The pellet was re-homogenized and centrifuged to increase the yield of mitochondria. Mitochondria-containing supernatants were pooled and centrifuged at 15000 g for 2 minutes to pellet mitochondria. The supernatant was collected as the cytosolic fraction. The mitochondrial pellet was washed three times using ice-cold homogenization buffer (10 mM Tris-HCl pH 7.4, 1 mM EDTA, 0.32 M sucrose).

Cytosolic mtDNA measurement

The protocol of measuring cytosolic mtDNA of BJ fibroblasts was adapted from a published assay.[73] In short, cells were grown in 10 cm culture dishes to reach 80-90% of confluency, harvested by trypsin digestion, and resuspended in 1 mL of PBS on ice. A small fraction of cells (50 μL) was directly lysed in 50 μL of RIPA buffer for measuring proteins using western blot or in 50 μL of the DNA extraction buffer (10 mM Tris-HCl pH 8.3, 50 mM KCl, 2.5 mM $MgCl_2$, 0.45% NP-40, 0.45% Tween-20, 0.01% gelatin, 200 μg/mL proteinase K. Lyse at 60 °C 1 hour, then 95 °C for 15 minutes.) for measuring total mtDNA as the input control. The remaining cells were resuspended in 600 μL of the digitonin lysis buffer (50 mM HEPES, pH 7.4, 150 mM NaCl, 18 μg/mL digitonin, 1X protease inhibitor cocktail) and incubated on a tube rotator for 10 minutes at 4 °C to allow mild plasma membrane permeabilization. To more efficiently release cytosolic components, the lysates were homogenized using a glass Dounce homogenizer on ice for 20 strokes. The homogenized lysates were centrifuged at 1,000 g for 3 minutes to remove cellular debris and large organelles. The supernatants were centrifuged again at 20,000 g for 3 minutes to fully remove mitochondria. To measure mtDNA using qPCR, 0.45 μL of the cytosolic supernatant or 0.02 μL of the whole cell lysate were used in each 10 μL reaction. For comparison between different samples using the ΔΔCt method, Ct values of the cytosolic mtDNA were first normalized to the total mtDNA input of the same culture dish measured using whole cell lysates and then to the control group.

ATP measurement

The CellTiter-Glo 2.0 luminescence assay kit (G9242, Promega) was used to measure cellular ATP levels according to manufacturer's protocol. In brief, cells of identical numbers for each condition were plated in a dark-walled 96-well plate (3904, Corning) and grown overnight to reach the confluency of 80%. The plate was equilibrated to room temperature for 30 minutes and an equal volume (100 μL) of the CellTiter-Glo 2.0 reagent was added to each well. The contents were mixed for 10 minutes on an orbital shaker at room temperature protected from light. The luminescence was measured using a Tecan Infinite M1000 plate reader (Tecan).

Lentiviral transduction for expressing vectors in BJ cells

Vectors were transduced into target fibroblasts using lentiviral transduction. To generate lentivirus, 293T cells were grown in multi-well plates (Corning) to reach a 50% confluence level. For one well in a 6-well plate, 750 ng of the 3G pack mix and 750 ng of the target vector were mixed into 125 μL Opti-MEM (31985088, Thermo Fisher) with 5 μL P3000 (L3000001, Thermo Fisher). In a separate tube, 5 μL Lipofectamine 3000 (L3000001, Thermo Fisher) was added into 125 μL Opti-MEM. This Lipofectamine mixture was then mixed with the DNA/Opti-MEM blend and incubated for 10 minutes at room temperature before being added to the 293T cells. After 1 day, 3 mL of fresh culture media was added. The supernatant that contains virus was collected 3 days post transfection by filtering through a 0.45 μm syringe filter unit and used freshly or stored at 4 °C to -80 °C.

For transduction, BJ fibroblasts were grown in multi-well plates to reach 50% of confluency. Filtered media containing lentivirus were directly added to the BJ cell culture. To increase the transduction efficiency, 2 μg/mL of polybrene (sc-134220, Santa Cruz) was added to the culture system. Selective antibiotics (1 μg/mL Puromycin (A11138, Thermo Fisher), 400 μg/mL Geneticin (10131027, Thermo Fisher); 5 μg/mL Blasticidin (A11139, Thermo Fisher)) were added to transduced BJ cells 2 days after transduction. Cells were grown with antibiotics for 1-2 weeks depending on the efficiency of the selection. As a negative control, antibiotic-sensitive wild-type BJ cells were treated with antibiotics to monitor the efficiency of selection.

CRISPR-KO screen

To validate the editing efficiency, Cas9-expressing BJ fibroblasts were transduced with a self-cutting plasmid that expresses a GFP reporter and an sgRNA that targets the GFP sequence. After puromycin selection, cellular fluorescence was measured using Incucyte. The absence of GFP fluorescence in cells indicates a successful knockout.

To generate the CRISPR-KO screening library, sgRNAs targeting a total of 2073 genes, including all known cell surface proteins using CRISPick,[78] along with 1708 control sgRNAs were synthesized by Twist Bioscience and cloned into pMCB320 using BstXI/BlpI overhangs after PCR amplification (see Table S1 for complete list of genes and sgRNAs).[79,80] The gene list was obtained from the Human Protein Atlas open access resource under the subcellular section of ''plasma membrane''. This library was transduced into Cas9-expressing cell lines and selected for with puromycin for 7 days.

After puromycin selection, cells were expanded to 10 million for each condition (T0), then treated with basic culture media, 600 ng/mL rotenone, or CF media. For rotenone or CF treatment, cells were grown under stress conditions at the starting confluency of 30% for 3 days, which was followed by 4 days of recovery and expansion in basic culture media. This stress-recovery cycle were repeated for 3 times. As the basal control, cells were grown in basic culture media for 3 weeks with routine 1:8 split when grown to 90% of confluency.

At the end of the screen, genomic DNA from 10 million cells of each condition was extracted using QIAamp DNA Blood Midi kit (51183, Qiagen). The sgRNAs were amplified and prepared for sequencing with a previously described nested PCR protocol with slight modification to make sgRNA sequencing library compatible with Illumina read 1 primer. Briefly, the sgRNA-encoding constructs were first amplified with primers oMCB1562 and oMCB1563, followed by a second PCR to introduce staggered sequences and indices for multiplexing (see Table S2 for primer sequences). The PCR products obtained were subjected to gel purification before being sequenced on the Illumina HiSeq platform. Hits identification was carried out using casTLE.[81] The signed casTLE scores, referred to as ''GeneEnrichment'' scores'', were employed for depicting figures.

To calculate casTLE scores for basal growth, basal growth control samples were normalized to T0 samples. To calculate casTLE scores for CF or rotenone treatment, stress-treated samples were normalized to basal growth samples. The normalized castle scores can be found in Table S1.

Quantification of mitochondrial features in images using Fiji

To count the number of mitochondrial puncta structures in images of fibroblasts, mitochondrial images were filtered using the ''Gaussian Blur'' function with the sigma values being 20 and 1 respectively. The ''subtract create'' image calculator function was used to subtract pixel values of the first filtered image from the second filtered image. This step helps define puncta structures. The new image was then filtered using the ''AutoThreshold (MaxEntropy dark)'' function to eliminate background signals. The ''Analyze Particles'' function was used with the parameters of size=1-Infinity, circularity=0.50-1.00 to count the number of mitochondria puncta.

To measure mitochondrial length in images of mitochondrial reporter worms, Z-stack images were first projected into a single layer using the ''Average Intensity'' function. The ''Auto Local Threshold'' function was applied with parameters of ''method=Bernsen radius=15 parameter_1=0 parameter_2=0 white'' to define the mitochondrial signal region. The ''Skeletonize (2D/3D)'' function was applied to mark the position of each single mitochondrion and the "Analyze Skeleton (2D/3D)" function was applied to measure the length as well as other parameters of these mitochondrial skeletons.

QUANTIFICATION AND STATISTICAL ANALYSIS

The Prism 9 software (GraphPad) was used for statistical analyses. Data are represented as mean ± SEM unless otherwise specified. All data points refer to the measurement of distinct samples (biological repeats). Unpaired two-tailed Student's t test was used for comparisons between two normally distributed datasets with equal variances unless specified. Welch's unequal variances t test was used when the two normally distributed datasets have unequal variances. Unpaired one/two-way ANOVA, followed with post hoc Dunnett's test (comparing multiple means with the single control group), or Tukey's test (comparing the mean of each sample with the mean of every other sample), was used for multiple comparisons of normally distributed datasets with one/two variables. Mann-Whitney U test was used for comparisons between non-parametric datasets. Kruskal-Wallis test with post hoc Dunn's test was used for multiple comparisons between non-parametric datasets or datasets with unequal variances. Log-rank (Mantel-Cox) test was used to compare lifespans between two groups of worms. P values were used to quantify the statistical significance of the tests.

ADDITIONAL RESOURCES

Graphics

Biorender and Microsoft PowerPoint were used for generating cartoon graphics. Prism 9 and R were used for generating data graphics.

Supplemental figures

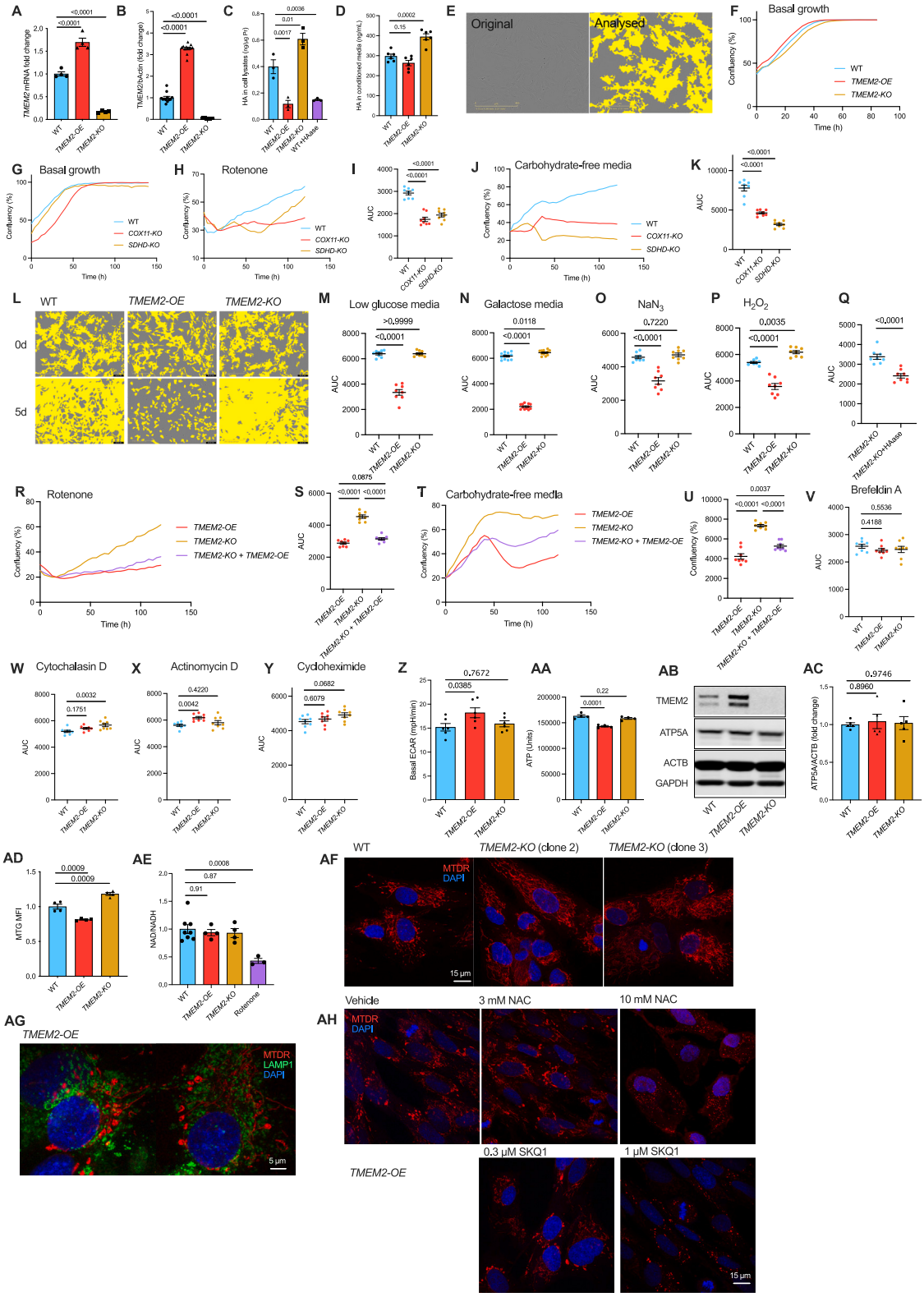

(legend on next page)

Figure S1. TMEM2 induces mitochondrial remodeling, related to Figure 1

(A) The mRNA levels of *TMEM2* in WT, *TMEM2-OE*, and *TMEM2-KO* BJ fibroblasts were measured by qPCR. $n = 4$.

(B) The protein levels of TMEM2 in WT, *TMEM2-OE*, and *TMEM2-KO* BJ fibroblasts were measured by western blot and the quantification result is shown. $n = 4$.

(C and D) HA in cell lysates (C) or conditioned culture media (D) was measured by ELISA and normalized to cell amount quantified by the BCA assay. Hyaluronidase (HAase) was added to the cell culture at the concentration of 2 mg/mL for 24 h. $n = 3–6$.

(E and F) Cellular growth was monitored using Incucyte live-cell imaging and quantified by cell confluency. One example of an original image and an analyzed image is shown (E). Cells were grown in standard culture media and their growth curves were shown in (F).

(G–K) *COX11-KO* or *SDHD-KO* cells were grown in standard culture media (G), or treated with rotenone (H and I), or grown in carbohydrate-free (CF) media (J and K). Cellular growth was measured using Incucyte (G, H, and J) and growth curves were compared using AUC values (I and K). $n = 8$.

(L) Cells of indicated genotypes were grown in CF media for 0 or 5 days in Incucyte. One representative image for each condition is shown.

(M–Q) Cells were grown in low-glucose (0.2 g/L glucose) media (M), galactose media (N), or treated with NaN_3 (O), H_2O_2 (P), or HAase with rotenone (Q) for 4 days. Cellular growth was monitored by Incucyte and growth curves were compared using AUC values. $n = 8–12$.

(R–U) The protospacer adjacent motif (PAM)-mutated *TMEM2* was overexpressed in *TMEM2-KO* cells. Cellular resistance against rotenone (R and S) or CF media (T and U) was assessed by Incucyte. $n = 8$.

(V–Y) Cells were treated with brefeldin A (V), cytochalasin D (W), actinomycin D (X), cycloheximide (Y). Cellular growth was monitored by Incucyte for 4 days and quantified by AUC. $n = 8$.

(Z) The basal extracellular acidification rate (ECAR) was measured using Seahorse. $n = 6$.

(AA) Cellular ATP amounts were measured using CellTiter-Glo 2.0. $n = 4$.

(AB and AC) ATP5A of indicated cell types was measured by western blot (AB) and quantified in (AC). $n = 5$.

(AD) Cells were stained with MTG and analyzed using flow cytometry. $n = 4$.

(AE) Cellular NAD and NADH were measured using the NAD/NADH-Glo Assay Kit. $n = 3–8$.

(AF) Cells were stained with MTDR and imaged using an Airyscan confocal microscope. One representative image for each cell line is shown. The clone 1 is shown in Figure 1K and referred to as "*TMEM2-KO*" in this study.

(AG) *TMEM2-OE* cells were stained with MTDR, DAPI, and an antibody against LAMP1. Two representative images acquired using an Airyscan confocal microscope are shown.

(AH) *TMEM2-OE* cells were treated with N-acetyl-L-cysteine (NAC) or SKQ1 at indicated concentrations for 24 h, followed by MTDR staining and Airyscan imaging. One representative image for each condition is shown.

Data represented as mean only (growth curves) or mean ± SEM. One-way ANOVA with post hoc Dunnett's test (A–P and V–AE), post hoc Tukey's test (S and U), or Student's t test (Q).

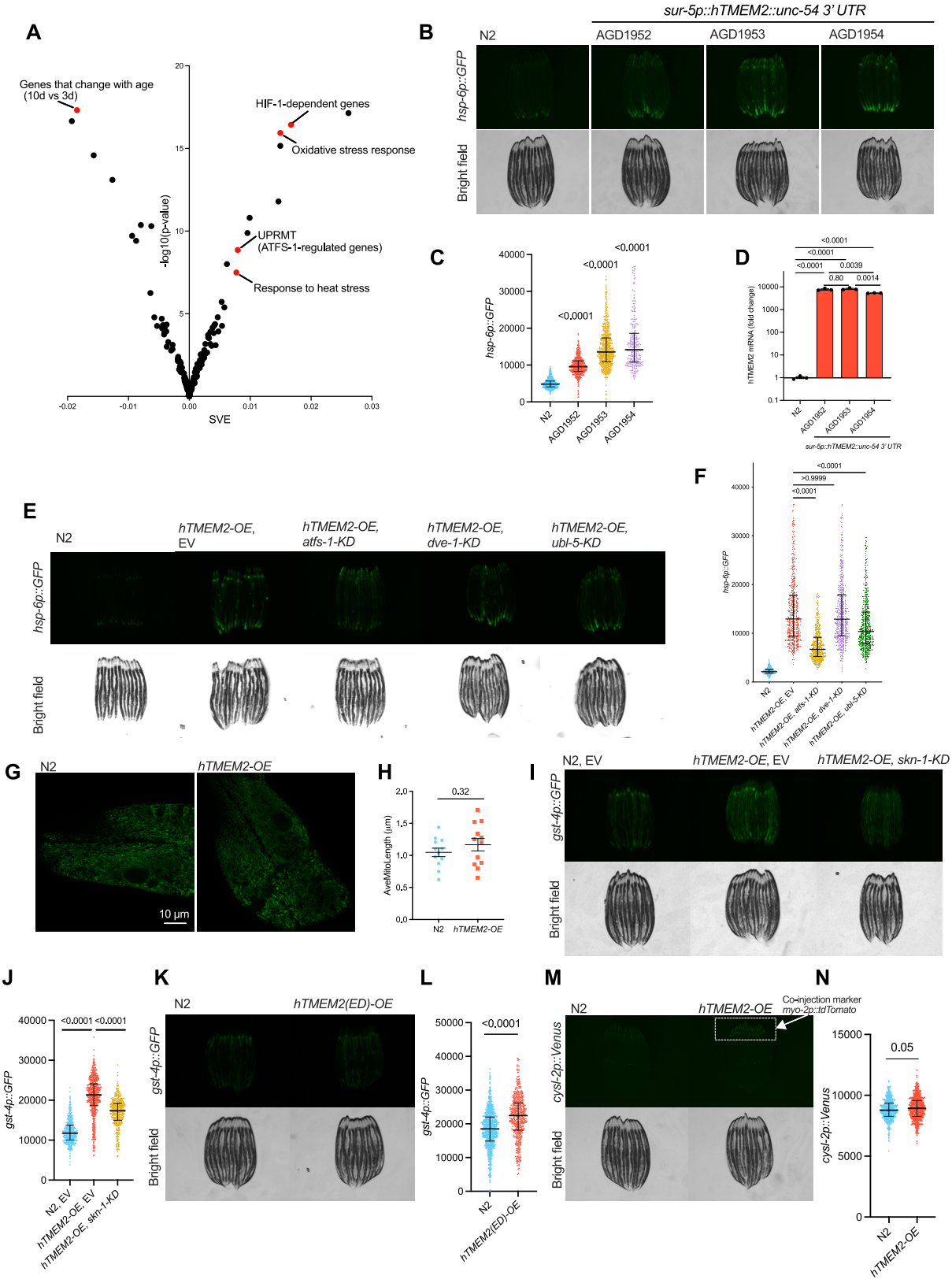

(legend on next page)

Figure S2. TMEM2 induces UPR^{MT} in an *atfs-1*-dependent manner, related to Figure 2

(A) RNA-seq datasets of D2 adult N2 (wild-type) and *hTMEM2-OE* (*sur-5p::hTMEM2*) animals were analyzed by comparing gene changes to a module-definition matrix that contains weights of every gene in different functional modules. SVE, signed variance explained (*hTMEM2-OE* vs. N2).

(B–D) A total of three stable *hTMEM2-OE* animal lines (AGD1952, AGD1953, and AGD1954) were generated by UV integration. These lines were crossed with the *hsp-6p::GFP* UPR^{MT} reporter strain, imaged using fluorescence microscopy (B), and quantified with a worm sorter (C). The expression levels of *TMEM2* in each line were measured by qPCR (D). The AGD1953 line is referred to as the "*hTMEM2-OE*" strain in this study. *n* = 296–702.

(E and F) *hTMEM2-OE hsp-6p::GFP* reporter animals were grown on EV or indicated RNAi bacteria, followed by GFP measurement using fluorescence microscopy (E) and a worm sorter (F). *n* = 575–694.

(G and H) *hTMEM2-OE vha-6p::MLS::GFP* mitochondrial reporter animals were imaged using an Airyscan confocal microscope at the age of D1 (G). Individual mitochondrial length was measured using FIJI (H). *n* = 12.

(I–L) *hTMEM2-OE gst-4p::GFP* or *hTMEM2(ED)-OE gst-4p::GFP* reporter animals were grown on empty vector (EV) control or *skn-1* RNAi bacteria, followed by GFP measurement using fluorescence microscopy (I and K) and a worm sorter (J and L). *n* = 375–836.

(M and N) *hTMEM2-OE* animals were crossed with the *cysl-2p::Venus* HIF-1 reporter strain and imaged using fluorescence microscopy (M) or quantified with a worm sorter (N). *n* = 478–515.

Data represented as median ± interquartile range (C, F, J, L, and N) or mean ± SEM (D and H). Kruskal-Wallis test with post hoc Dunn's test (C, F, and J), one-way ANOVA with post hoc Tukey's test (D), Student's t test (H), or Mann-Whitney test (L and N).

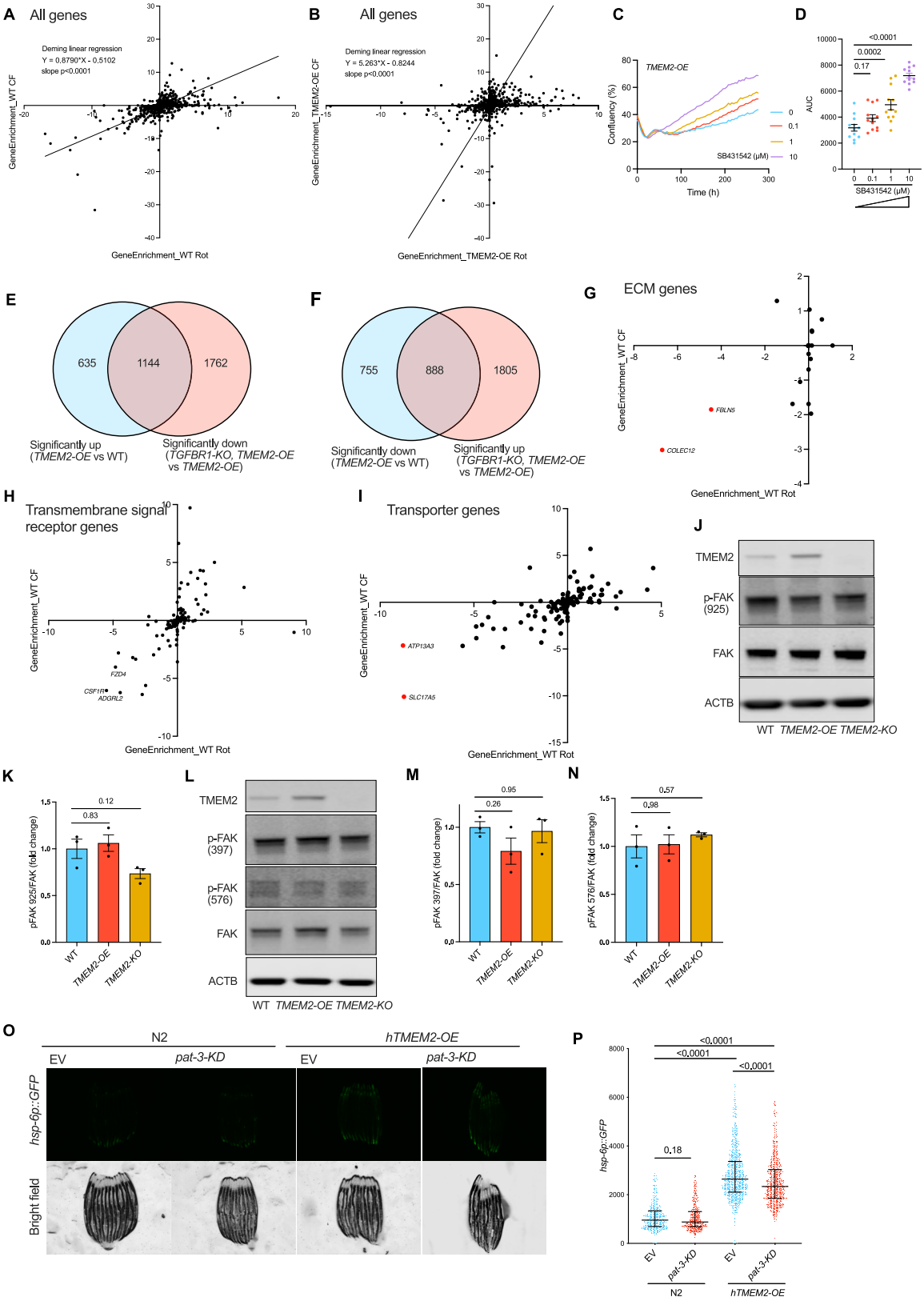

(legend on next page)

Figure S3. Mitochondria-regulating genes identified by a CRISPR-KO screen, related to Figure 3

(A and B) Display of gene enrichment scores of WT cells (A) or *TMEM2-OE* cells (B) after CF or rotenone selection.

(C and D) *TMEM2-OE* cells were treated with SB431542 at indicated concentrations for rotenone stress resistance assays using Incucyte (C). AUC values were calculated for statistical analyses (D). $n = 12$.

(E and F) RNA-seq was performed on WT, *TMEM2-OE*, and *TGFBR1-KO TMEM2-OE* fibroblasts. Significantly up-regulated (E) or down-regulated (F) genes (p-adj < 0.05) of the *TMEM2-OE* vs. WT comparison are compared with significantly changed genes in the *TGFBR1-KO TMEM2-OE* vs. *TMEM2-OE* comparison and summarized in Venn diagrams. $n = 4$.

(G–I) Display of gene enrichment scores of WT cells after CF or rotenone selection. The ECM genes are selectively shown in (G). The transmembrane signal receptor genes are selectively shown in (H). The transporter genes are selectively shown in (I).

(J–N) Total and phosphorylated forms of FAK in WT, *TMEM2-OE*, and *TMEM2-KO* cells were measured by western blot and quantified using Image Studio Lite. $n = 3$.

(O and P) UPR^{MT} reporter animals with WT or *hTMEM2-OE* genetic background were grown on EV or *pat-3* RNAi bacteria. GFP was measured by fluorescence microscopy (O) and a worm sorter (P). $n = 378–828$.

Data represented as mean (C), mean ± SEM (D, K, M, and N), or median ± interquartile range (P). One-way ANOVA with post hoc Dunnett's test (D, K, M, and N) or Kruskal-Wallis test with post hoc Dunn's test (P).

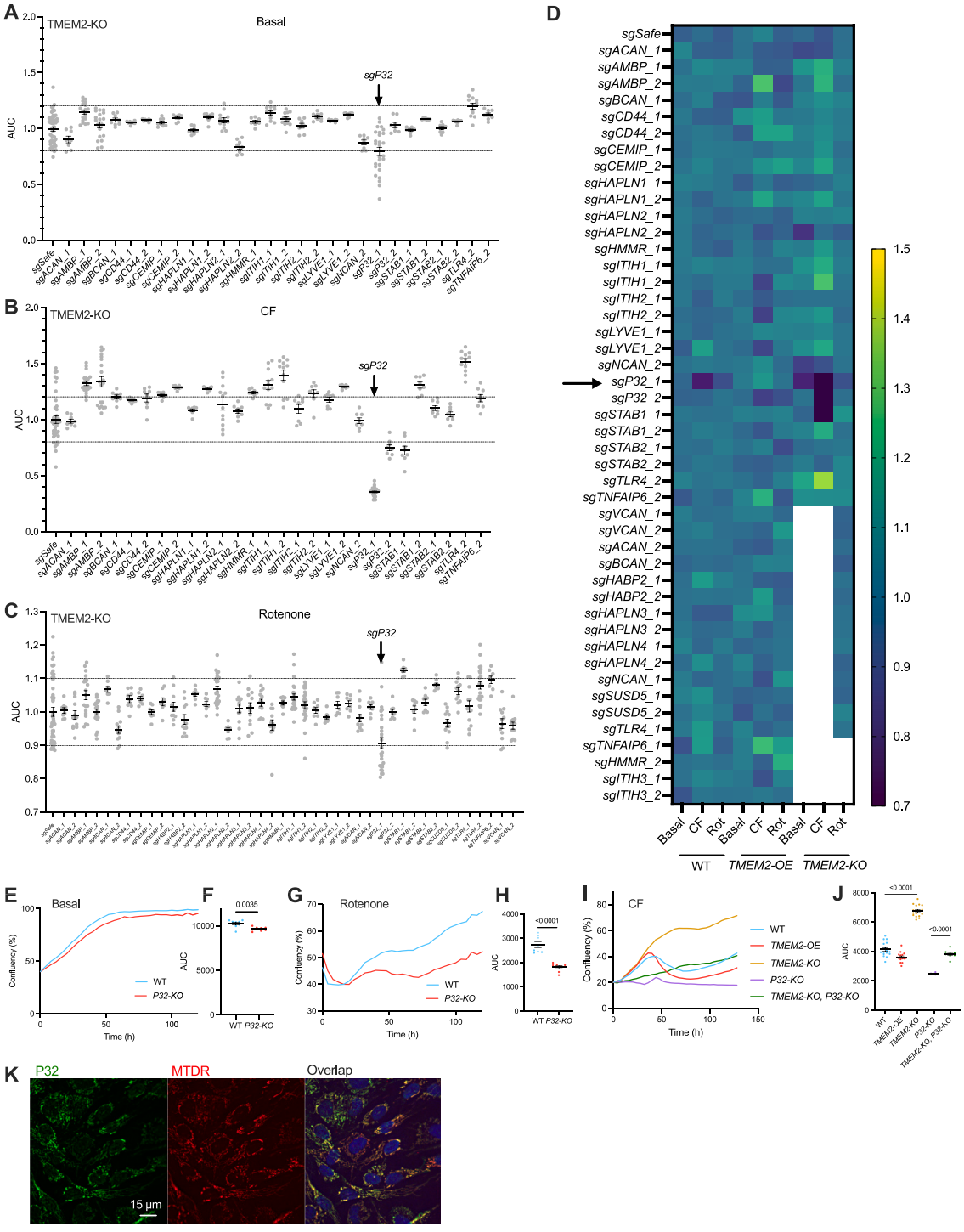

Figure S4. HABPs do not mediate the TMEM2-mitochondria crosstalk, related to Figure 3

(A–C) Indicated HABP genes were knocked out in Cas9-expressing *TMEM2-KO* cells. Two different sgRNA sequences were designed for each gene. Cellular growth of each individual line was monitored in 96-well plates using Incucyte under basal conditions (A), CF media treatment (B), or rotenone treatment (C). AUC values for each growth curve were normalized to the *sgSafe* (safe-targeting) line for comparison. The strongest hit *sgP32_1* is highlighted with an arrow. $n = 8–52$. (D) Similar to *TMEM2-KO* cells in (A)–(C), HABP genes were knocked out in WT and *TMEM2-OE* cells for testing mitochondrial stress resistance. Normalized mean AUC values for each condition were summarized in a heatmap. The strongest hit *sgP32_1* is highlighted with an arrow.

(legend continued on next page)

(E–J) Cells of indicated genotypes were grown under basal conditions (E and F), with rotenone (G and H), or in CF media (I and J). Cellular growth was monitored using Incucyte (E, G, and I) and AUC values calculated for comparison (F, H, and J). n = 8–16.
(K) WT cells were stained with MTDR, DAPI, and a P32 antibody for fluorescence microscopy imaging. One representative image is shown.
Data represented as mean ± SEM (A–C, F, H, and J) or mean only (D, E, G, and I). Student's t test (F and H) or one-way ANOVA with post hoc Tukey's test (J).

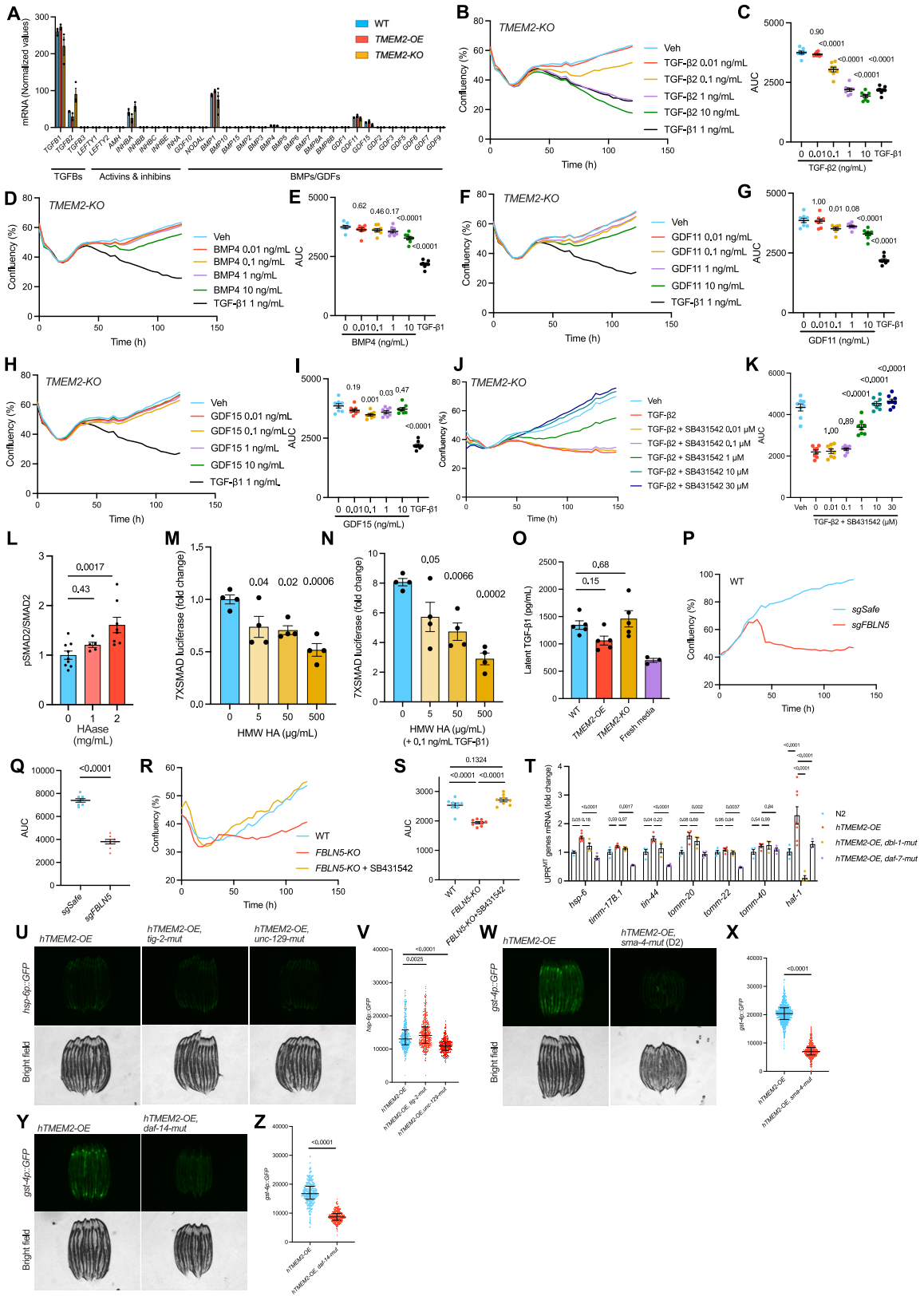

(legend on next page)

Figure S5. TGF-β regulates mitochondrial homeostasis, related to Figure 4

(A) The expression of TGF-β superfamily genes in WT, *TMEM2-OE*, and *TMEM2-KO* cells was analyzed from published RNA-seq datasets. *n* = 2–3.

(B–K) *TMEM2-KO* cells were treated with indicate TGF-β superfamily ligands and/or SB431542 at indicated concentrations for rotenone stress resistance tests using Incucyte (B, D, F, H, and J). AUC values were calculated for statistical analyses (C, E, G, I, and K). *n* = 8.

(L) Quantification of Figure 4J. *n* = 5–9.

(M and N) The 7XSMAD luciferase reporter BJ cells were treated with HMW HA alone (M) or together with 0.1 ng/mL TGF-β1 (N) for 6 h, followed by the luciferase activity assay. Luminescence values were normalized to the average of the 0 HMW HA group in (M). *n* = 4.

(O) TGF-β1 in conditioned culture media of indicated cell types was measured by ELISA. *n* = 3–5.

(P–S) *FBLN5* was knocked out in BJ fibroblasts for CF resistance tests (P and Q) or rotenone stress resistance tests (R and S) using Incucyte. SB431542 was added at the concentration of 10 μM (R and S). *n* = 8.

(T) Wild-type, *hTMEM2-OE*, *hTMEM2-OE dbl-1-mut*, and *hTMEM2-OE daf-7-mut* animals were grown on EV bacteria until the day 1 adult stage and harvested for measuring UPR^{MT} genes using qPCR. *n* = 4–8.

(U and V) *hTMEM2-OE hsp-6p::GFP* reporter animals were crossed with indicated TGF-β ligand mutant strains and GFP measured using fluorescence microscopy (U) and a worm sorter (V). *n* = 429–628.

(W–Z) *hTMEM2-OE gst-4p::GFP* reporter animals were crossed with indicated TGF-β pathway mutant strains and GFP measured using fluorescence microscopy (W and Y) and a worm sorter (X and Z). *n* = 228–1,444.

Data represented as mean only (B, D, F, H, J, P, and R), mean ± SEM (A, C, E, G, I, K–O, Q, S, and T), or median ± interquartile range (V, X, and Z). One-way or two-way ANOVA with post hoc Dunnett's test (C, E, G, I, K–O, and T) or post hoc Tukey's test (S), Student's t test (Q), Kruskal-Wallis test with post hoc Dunn's test (V), or Mann-Whitney test (X and Z).

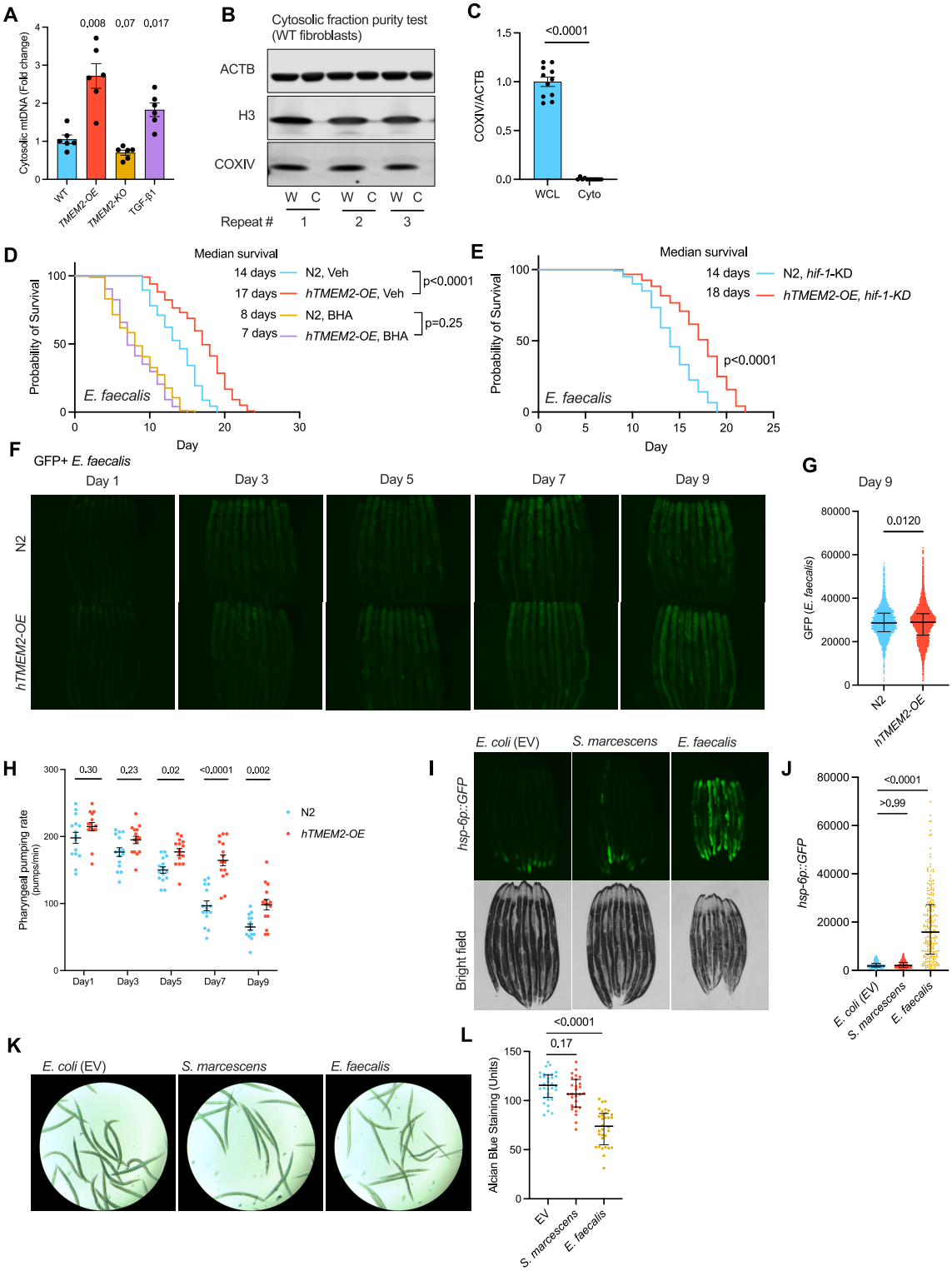

Figure S6. TMEM2 promotes animal immunity, related to Figure 6

(A–C) The whole-cell lysate (W, WCL) or the cytosolic fraction (C, Cyto) of cells was isolated for mtDNA measurement by qPCR (A) or for protein measurement by western blot (B), which is quantified in (C). *n* = 6–11.

(D) Animals were hatched on EV bacteria supplemented with 1 mM BHA or vehicle and grown to the L4 stage; they were then transferred to *E. faecalis* bacteria supplemented with 1 mM BHA or vehicle for lifespan measurement. *N* = 120.

(legend continued on next page)

(E) Animals were hatched on *hif-1* RNAi bacteria and grown to the L4 stage; they were then transferred to *E. faecalis* bacteria mixed with RNAi bacteria for lifespan measurement. *N* = 120.

(F–H) Animals were hatched on EV bacteria and grown to the L4 stage; they were then transferred to GFP+ *E. faecalis* bacteria and imaged on indicated adult stages (F) and quantified using a worm sorter (G). *n* = 2,722–6,710. The pharyngeal pumping rate was counted under a stereo microscope at indicated adult stages (H). *n* = 15.

(I and J) Animals were hatched on EV bacteria and grown to the L3 stage; they were then transferred to pathogenic bacteria, imaged at the day 3 adult stage (I), and quantified using a worm sorter (J). *n* = 205–655.

(K and L) L1 synchronized N2 animals were grown on indicated bacteria at 20°C for 46 h and stained with Alcian blue. Images were taken with a color sensor-equipped Revolve microscope (K) and quantified using FIJI (L). *n* = 27–32.

Data represented as mean ± SEM (A, C, and H) or median ± interquartile range (G, J, and L). One-way ANOVA with post hoc Dunnett's test (A and L), Mann-Whitney test (C and G), log-rank test (D and E), two-way ANOVA with post hoc Šídák's test (H), or Kruskal-Wallis test with post hoc Dunn's test (J).